

Instability triggered by mixed convection in a thin fluid layer

Florian Rein^{1,2†}, Keaton J. Burns^{3,4}, Stefan G. Llewellyn Smith^{2,5},
William R. Young², Benjamin Favier¹ and Michael Le Bars¹

¹Aix Marseille Université, CNRS, Centrale Med, IRPHE, Marseille, France

²Scripps Institution of Oceanography, University of California San Diego, La Jolla, CA 92093, USA

³Department of Mathematics, Massachusetts Institute of Technology, Cambridge, MA 02139, USA

⁴Center for Computational Astrophysics, Flatiron Institute, New York, NY 10010, USA

⁵Department of Mechanical and Aerospace Engineering, Jacobs School of Engineering, University of California San Diego, La Jolla, CA 92093, USA

(Received xx; revised xx; accepted xx)

We investigate the convective stability of a thin, infinite fluid layer with a rectangular cross-section, subject to imposed heat fluxes at the top and bottom and fixed temperature along the vertical sides. The instability threshold depends on the Prandtl number as well as the normalized flux difference (f) and decreases with the aspect ratio (ϵ), following a ϵf^{-1} power law. Using 3D initial value and 2D eigenvalue calculations, we identify a dominant 3D mode characterized by two transverse standing waves attached to the domain edges. We characterize the dominant mode's frequency and transverse wave number as functions of the Rayleigh number and aspect ratio. An analytical asymptotic solution for the base state in the bulk is obtained, valid over most of the domain and increasingly accurate for lower aspect ratios. A local stability analysis, based on the analytical base state, reveals oscillatory transverse instabilities consistent with the global instability characteristics. The source term for this most unstable mode appears to be interactions between vertical shear and horizontal temperature gradients.

Key words:

1. Introduction

The present work follows the numerical study of Rein *et al.* (2023) and the experimental study of Rein *et al.* (2025), which was motivated by nuclear safety issues (see Rein *et al.* (2024)). During a severe accident in a nuclear power plant, the radioactive fuel and metallic components of the reactor melt, forming a fluid known as corium. The corium moves from the reactor core to the lower plenum of the reactor vessel, where non-miscible oxidic and metallic phases separate. The oxide phase contains the majority of the radioactive elements and provides heat from below to the less dense and thinner liquid metal phase floating on its surface, which then focuses the heat towards the vessel wall. This phenomenon is referred to as the “focusing effect” in the nuclear safety literature. Understanding heat transfer through the top metal layer is essential for evaluating the

† Email address for correspondence: florian.rein@protonmail.com

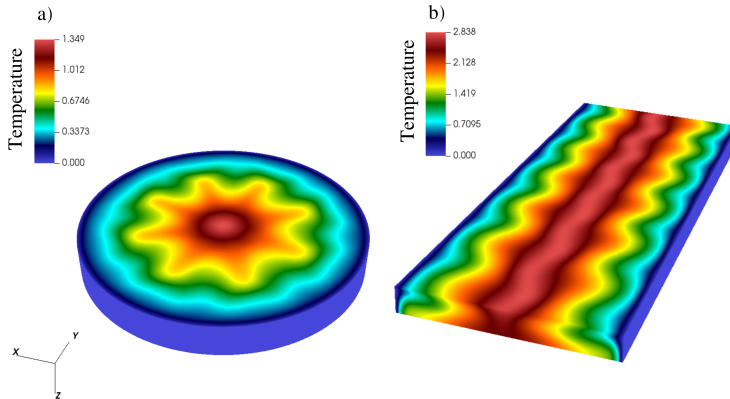


FIGURE 1. Snapshot of the bottom temperature field in a (a) cylindrical with $Ra = 2 \times 10^4$ and (b) Cartesian geometry with $Ra = 2 \times 10^3$. For both cases, the parameters are $\epsilon = 1/4$, $Pr = 0.1$ and $f = 0.9$. To mimic the homogeneous azimuthal direction of the cylindrical case, periodic boundary conditions are applied in the transverse direction for the Cartesian case. Parameters and boundary conditions will be detailed in [section 2](#).

risk of vessel failure and ensuring its integrity when “in-vessel retention” is employed as a severe accident management strategy ([Theofanous *et al.* 1997](#); [Carénini *et al.* 2018](#)).

Our previous study of the turbulent metal layer dynamics ([Rein *et al.* 2023](#)) used DNS of a thin cylindrical layer heated from below and cooled from above with imposed fluxes and cooled from the side with imposed temperature. It highlighted the presence of a three-dimensional (3D) drifting thermal structure composed of hot radial branches (see e.g. [Figure 1\(a\)](#)) which plays a crucial role in the spatiotemporal structure of heat transfer fluctuations. This drifting structure was further confirmed experimentally by [Rein *et al.* \(2025\)](#). The physical mechanisms behind the emergence of this pattern are so far unknown. It should be noted that this instability is not specific to the cylindrical geometry, but persists in Cartesian geometry, the focus of this paper. [Figure 1](#) illustrates this point with two simulations performed using the same parameters but in cylindrical and Cartesian geometries.

In our system, a mixture of different types of convection can be expected. Bottom heating and top cooling are reminiscent of Rayleigh-Bénard configurations for which it is known that there exists a threshold below which diffusive processes dominate over buoyancy forces, leading to a stable motionless base state ([Chandrasekhar 1981](#)). The appearance and nonlinear dynamics of different patterns and structures above onset have been extensively studied both theoretically ([Busse 1978](#); [Busse & Clever 1979](#); [Golubitsky *et al.* 1984](#)) and experimentally ([Caldwell 1970](#); [Krishnamurti 1970](#); [Bruyn *et al.* 1996](#)). The case where the heat flux through the top is equal to the heat flux through the bottom was notably investigated by [Chapman & Proctor \(1980\)](#) and [Gertsberg & Sivashinsky \(1981\)](#). If the heat flux through the top is less than the heat flux through the bottom, then in steady state and in the absence of internal cooling, there must be an additional heat flux through the lateral boundaries (sidewalls). This lateral cooling implies a horizontal temperature gradient which cannot be balanced by a hydrostatic pressure gradient. In this problem of natural convection the critical Rayleigh number is zero, i.e. an arbitrarily small vertical flux imbalance induces convective motion.

Theoretical studies have examined the two-dimensional case in a closed box with insulated rigid walls at the top and bottom and differing imposed sidewall temperatures. [Cormack *et al.* \(1974\)](#) considered small aspect ratio cases and showed, using matched

asymptotic expansions, that the 2D flow consists of two distinct regimes: a parallel flow in the core region and a second non-parallel flow near the ends of the cavity. A solution valid at all orders in the aspect ratio was found for the core region, while the first several terms of the appropriate asymptotic expansion were obtained for the end regions. In the opposite asymptotic limit of a tall box, Gill (1966) found a 2D approximate solution for the velocity and temperature fields compatible with the vertically infinite solution of Batchelor (1954). Low Prandtl regime dynamics has been investigated theoretically by Hart (1983); a core solution, asymptotically valid at small aspect ratio was found, breaking down either as end effects extend into the center of the cavity or as a secondary shear flow instability develops in the core itself. The stability of this flow was investigated by Daniels *et al.* (1987) highlighting the role of the side boundary layer, as was further investigated by Daniels & Gargaro (1993).

The combination of these convection regimes referred to as “inclined” or “oblique” temperature gradient was examined by Weber (1978). Both vertical (similar to Rayleigh-Bénard) and horizontal (similar to natural convection) temperature gradients are specified. Weber (1978) considered the instability of the convective shear flow under the action of an inclined temperature gradient using a linear stability approach. He found that varying the horizontal and vertical temperature gradients caused the flow to become unstable to different types of disturbances. These included longitudinal rolls aligned with the flow, transverse traveling rolls, and their oscillations. Ortiz-Pérez & Dávalos-Orozco (2014, 2015) studied the different instability modes that can appear, depending on the relative strength of the horizontal/vertical temperature gradients as well as the Prandtl number. Patne & Oron (2022) and Dixit *et al.* (2024) recently noted the destabilizing effect of horizontal temperature gradients leading to oblique oscillating modes for Prandtl number less than one.

All these results have been found for a fixed horizontal temperature gradient. In our system, the horizontal temperature gradient is not prescribed but emerges dynamically from the mismatch between the heat fluxes at the top and bottom boundaries. The stability of such a system and the physical mechanisms underlying the growth of instabilities are still unknown. This paper presents a numerical and theoretical study of the instability onset in a thin, infinite fluid layer with a rectangular cross-section at low Prandtl number. The objectives of this study are: (i) To find analytical solutions in the stable regime describing the temperature and velocity fields in the asymptotic limit of a small aspect ratio; (ii) To characterize the properties of the dominant mode at the onset of instability as a function of the parameters; and (iii) To identify the potential physical mechanisms related to the emergence of the thermal pattern observed in the turbulent regime by Rein *et al.* (2023, 2025).

Section 2 outlines the governing equations and the numerical solvers employed. In section 3, we describe the base state by analyzing the flow structure and the different scalings involved in the low Rayleigh number regime, and propose an analytical asymptotic bulk solution. In section 4, we characterize the first instability in the system by examining the structure of the dominant mode and how its properties change with the input parameters. Additionally, we introduce a reduced model derived from the analytical asymptotic bulk solution, which successfully captures and reproduces the key characteristics of the instability. Finally we discuss the implications of our findings to identify the potential physical mechanisms behind the instability. We conclude in Section 5.

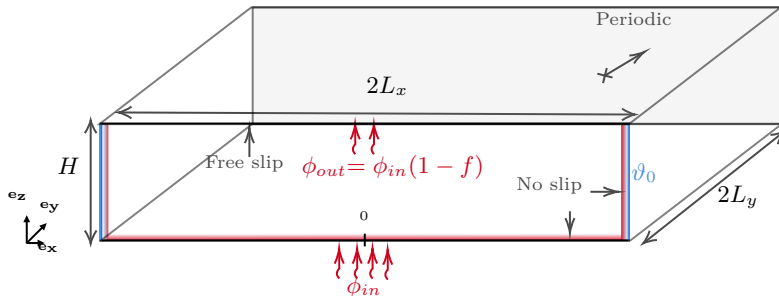


FIGURE 2. Sketch of the modeled fluid metal layer inside the box. Differing top and bottom fluxes are imposed while the sidewall temperatures are fixed and uniform.

2. Mathematical and numerical formulation

2.1. Governing equations

We consider the flow of an incompressible fluid under the Boussinesq approximation. The fluid is confined within a box of thickness H , length $2L_x$, periodic in the y -direction with period $2L_y$ (see Figure 2) and with gravity pointing downward: $\mathbf{g} = -g\mathbf{e}_z$. The fluid is heated from below with a uniform heat flux per unit area ϕ_{in} and cooled from above by a uniform outgoing flux ϕ_{out} . Note that we are interested in the cases where $\phi_{\text{in}} > \phi_{\text{out}}$ so that the residual heat flux necessarily escapes the domain through the sidewall boundaries at $x = \pm L_x$. The dimensional temperature on the x -side wall boundaries is fixed at ϑ_0 . We use no-slip boundary conditions at the bottom and lateral boundaries, and free-slip at the top boundary. Using a no-slip upper boundary condition does not qualitatively change the results discussed below. Lengths are rescaled using the height of the box H , while time is rescaled using the vertical diffusive timescale H^2/κ , with κ the constant thermal diffusivity. The dimensionless temperature T is defined relative to the imposed side temperature and rescaled using the imposed bottom flux ϕ_{in} , so that

$$T = \frac{k_{\text{th}}}{\phi_{\text{in}}H} (\vartheta - \vartheta_0) , \quad (2.1)$$

where k_{th} is the thermal conductivity. The dimensionless conservation equations for momentum, mass and energy are then

$$Pr^{-1} (\mathbf{u}_t + \mathbf{u} \cdot \nabla \mathbf{u}) = -\nabla P + RaT\mathbf{e}_z + \nabla^2 \mathbf{u} , \quad (2.2)$$

$$\nabla \cdot \mathbf{u} = 0 , \quad (2.3)$$

$$T_t + \mathbf{u} \cdot \nabla T = \nabla^2 T . \quad (2.4)$$

Here and from now on, A_α denote the partial derivative of A with respect to the variable α and \mathbf{u} , P and T are the dimensionless velocity, pressure and temperature of the fluid. The dimensionless boundary conditions can be written as

$$\begin{aligned} \mathbf{u} &= \mathbf{0} \quad \text{and} \quad T_z = -1 \quad \text{at} \quad z = 0 , \\ u_z = v_z = w &= 0 \quad \text{and} \quad T_z = -1 + f \quad \text{at} \quad z = 1 , \\ \mathbf{u} &= \mathbf{0} \quad \text{and} \quad T = 0 \quad \text{at} \quad x = \epsilon^{-1} , \end{aligned} \quad (2.5)$$

where $\mathbf{u} = (u, v, w)$ are the velocity components. The problem is characterized by four main dimensionless parameters: the aspect ratio ϵ , the normalized flux difference f , the Rayleigh number Ra based on the heat flux imposed at the bottom ϕ_{in} , and the Prandtl

number Pr . They are defined by

$$\epsilon = \frac{H}{L_x}, \quad f = 1 - \frac{\phi_{\text{out}}}{\phi_{\text{in}}}, \quad Ra = \frac{\beta g \phi_{\text{in}} H^4}{k \nu \kappa}, \quad Pr = \frac{\nu}{\kappa}, \quad (2.6)$$

where β is the thermal expansion coefficient and ν is the kinematic viscosity, both assumed to be constant. Added to this is the ratio L_y/H , fixed to 40 throughout the paper, which is large enough to ensure the natural development of the instability free from confinement effects along the y -direction. The present study explores the parameter space over a wide range, with ϵ varying from $1/8$ to $1/1024$, Ra from 3×10^{-2} to 1.5×10^4 , the normalized flux difference spanning $0.05 \leq f \leq 0.9$ and Pr from 0.1 to 1.0 . The lower bound $Pr = 0.1$ is chosen to represent metallic mixtures of zirconium, uranium oxide, and steel relevant to nuclear applications, for which Pr lies in the range 0.07 – 0.2 (Le Guennic *et al.* 2020), in line with previous studies. A complete list of the simulations performed is provided in [Appendix A](#).

The governing equations (2.2)–(2.4) with the boundary conditions (2.5) are solved using two primary methods. First, Direct Numerical Simulations (DNS) are employed to solve both 3D Initial Value Problems (IVPs), starting from given initial conditions and following their evolution in time, and 2D Boundary Value Problems (BVPs), which determine y -invariant steady-state solutions by solving (2.2)–(2.4) after removing temporal and y -derivatives. Second, an Eigenvalue Problem (EVP) approach is used to analyze the stability of these stationary solutions. Details of all methods are provided in [Appendix B](#).

2.2. Numerical approach

Two different numerical codes were used in this study. Dedalus is employed to determine the 2D base flows and temperature fields for each configuration via steady nonlinear boundary value problems (BVPs) and to investigate the stability of the system by solving global and local eigenvalue problems (EVPs). Nek5000 is used to perform 3D direct numerical simulations, solving initial value problems (IVPs) for given configurations.

2.2.1. Nek5000

The governing equations (2.2)–(2.4) with boundary conditions (2.5) and periodic boundary condition in the y direction, are solved using the spectral element code [Nek5000](#) (Fischer 1997; Deville *et al.* 2002) (IVP). The Cartesian geometry is discretized with up to $\mathcal{E} = 4096$ hexahedral elements, refined near all boundaries to resolve viscous and thermal boundary layers accurately. Numerical simulations are initiated with a quiescent fluid and a uniform temperature field $T = 0$ throughout the domain. Small random temperature perturbations of amplitude 10^{-3} are introduced, leading to thermal convection growth during a transient phase lasting ~ 10 vertical diffusive times, with longer durations observed for lower aspect ratios (ϵ). In order to test numerical convergence, we gradually increase the spectral polynomial order until convergence on the viscous dissipation is reached, as further described in [Rein *et al.* \(2023\)](#).

2.2.2. Dedalus

Background and stability calculations are conducted using Dedalus ([Burns *et al.* 2020](#)), a parallel pseudo-spectral solver. Our model uses a high-order continuous spectral element method on a 2D domain $(x, z) \in [0, L_x] \times [0, 1]$ to solve the y -invariant governing equations (2.2)–(2.4) with boundary conditions (2.5) and parity conditions imposed at $x = 0$. All fields are represented by bivariate Chebyshev expansions on a series of rectangular elements that expand dyadically away from the boundary as $[0, 0.5L_x]$, $[0.5L_x, 0.75L_x]$, ..., $[L_x - 4, L_x - 2]$, $[L_x - 2, L_x - 1]$, $[L_x - 1, L_x]$. Each element

employed up to $N_x \times N_z = 20 \times 20$ spectral modes and 3/2 dealiasing. This discretization is used to solve nonlinear boundary value problems (BVP) to determine steady base solutions via the Newton-Kantorovich method.

Global 3D eigenvalue problems (Global-EVP) are solved with the same discretization using the Dedalus eigentools extension (Oishi *et al.* 2021). These problems use a fixed set of parameters: Ra , Pr , ϵ and f across a range of k_y values from 10^{-2} to 5×10^1 . The same approach is applied to 2D local eigenvalue problems (Local-EVP), using the base solution’s vertical structure at a particular x as a uniform background, with the same parameters, but now across a range of k_y values from 0 to 2 and k_x values from -2 to 2. To ensure convergence, we verify that the eigenmode and eigenvalue of the most unstable case remain consistent even when the spectral resolution is doubled. For the sake of consistency, we compared the growth rates and mode structures from IVP simulations with Nek5000 against those obtained from the Global-EVP analysis using Dedalus.

A summary of all the numerical results involving each specific method, IVP, BVP, Global-EVP and Local-EVP, is given in Table 1 from Appendix A.

3. Base flow analysis

3.1. Qualitative overview

We begin with a qualitative description of the stationary two-dimensional base flow in the $(\mathbf{e}_x, \mathbf{e}_z)$ plane, obtained from IVP at steady state and for a very low $Ra_\phi = 10$, well below the instability threshold discussed later. We have checked that exactly the same results are obtained using the BVP approach using Dedalus. First, regardless of the control parameters, a motionless steady state does not exist in this system. Imposing different fluxes at the bottom and top boundaries generates a horizontal temperature gradient that cannot be balanced by a hydrostatic pressure gradient. This results in natural convection. Maintaining a constant temperature at the sides further reinforces this natural convection via a downward recirculation along the side boundary and a return flow toward the centre along the bottom boundary.

When temperatures are fixed on the top and bottom boundaries, the global recirculation covering the entire domain disappears, leaving only a vortex structure near the edge, as observed by Ganzarolli & Milanez (1995). This vortex structure, however, remains when heat fluxes are imposed at the top and bottom boundaries, extending over a penetration length similar to the layer thickness and independent of the aspect ratio, as shown in Figure 3. At low Ra (below the instability threshold discussed below), the flow and the temperature field are 2D, symmetric with respect to $x = 0$, and invariant along the y -direction (or axisymmetric in the cylindrical case). As the aspect ratio decreases, the influence of the side walls becomes confined to a smaller portion of the domain localized at the edges.

3.2. Scalings

In this section we fix $Pr = 0.1$ and $f = 0.9$, and seek scaling laws for the maximal temperature and horizontal velocity of the 2D base solution denoted T_{\max} and U_{\max} respectively, systematically varying Ra and ϵ . For each simulation, the steady state is computed using a BVP approach with Dedalus. The peak temperature is consistently located at the bottom centre, while the peak horizontal velocity is found at the top near the edge, just before the vortex recirculation area (see Figure 3). The evolution of these peak values with Ra and ϵ is shown in Figure 4.

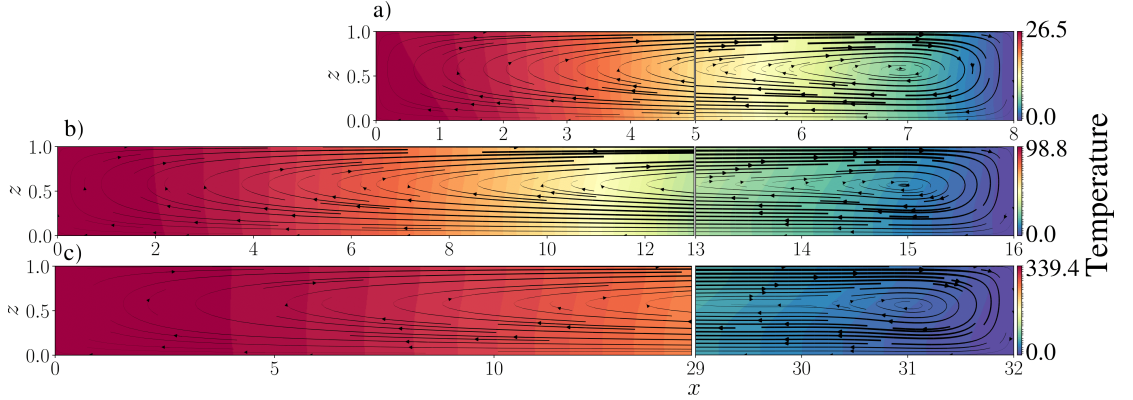


FIGURE 3. 2D view in a plane (x, z) of the temperature together with some velocity streamlines computed for aspect ratio (a) $1/8$, (b) $1/16$, (c) $1/32$. For each aspect ratio, a close-up view spanning three dimensionless units along the side wall is highlighted. The IVP method is used to obtain the data, which corresponds to the simulations IVP1 to IVP3 listed in Table 1. The parameters are $f = 0.9$, $Pr = 0.1$, $Ra = 10$.

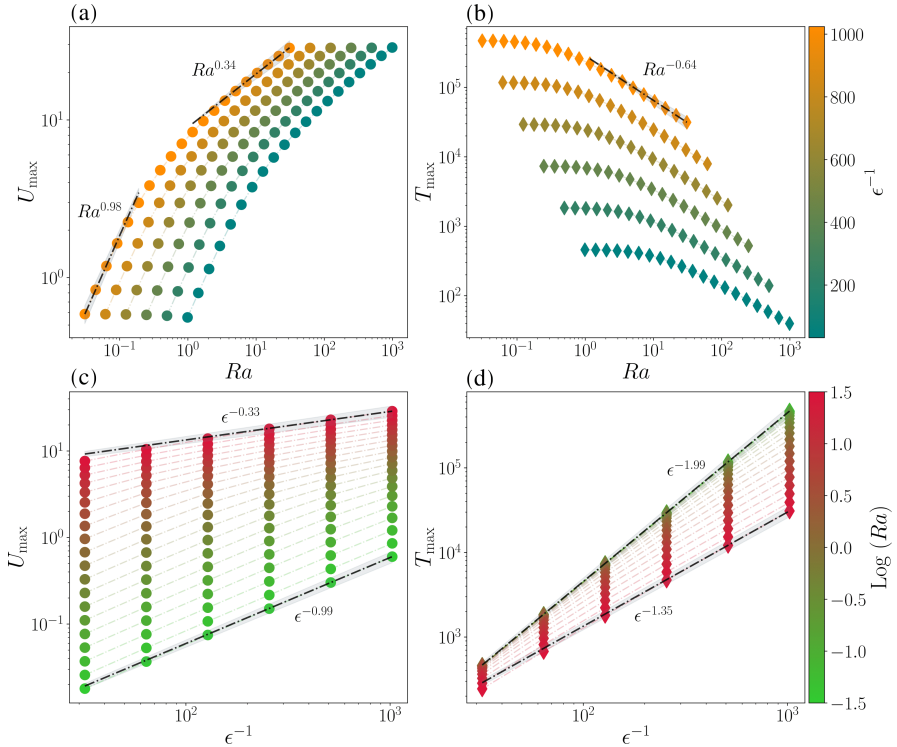


FIGURE 4. Peak values of (a), (c) horizontal velocity, (b), (d) temperature in the steady solution as a function of the Rayleigh number for aspect ratios from $1/1024$ to $1/32$ for Ra from 3×10^{-2} to 9.8×10^2 for a), b) and 3×10^{-2} to 3×10^1 for c), d). In each panel, the dash-dotted lines indicate the best-fit scaling law determined using a least squares method. The BVP method is used to obtain the data, corresponding to the simulations BVP1 to BVP6 listed in Table 1.

When the value of Ra increases at constant ϵ , the peak horizontal velocity also increases, while the peak temperature decreases as expected (see Figure 4(a,b)). This occurs because a higher Rayleigh number enhances heat transfer efficiency within the system, causing the average temperature to approach the side temperature, which is zero in our dimensionless units (2.1). Note, however, that the dimensional temperature increases with an increase in heat flux, Ra . We observe two main behaviors with Ra : at relatively low Ra , T_{\max} remains constant, while U_{\max} follows a power law behavior with an exponent unaffected by ϵ . Using a least squares method to estimate the power exponent, we find $U_{\max} \sim Ra^{0.98 \pm 0.01}$. To determine the mean exponent, we averaged the exponents for $\epsilon \in [1/32, 1/1024]$ considering only data where $U_{\max} \leq 2$, with variability quantified by the largest difference between these exponents. At higher Ra , both U_{\max} and T_{\max} follow a power law behavior in Ra with exponents unaffected by ϵ . Analyzing for each ϵ the 5 last Ra data points for U_{\max} and T_{\max} , using a similar method, gives $U_{\max} \sim Ra^{0.34 \pm 0.01}$ and $T_{\max} \sim Ra^{-0.64 \pm 0.03}$.

When ϵ decreases at constant Ra , U_{\max} and T_{\max} increase (see Figure 4(c,d)). Indeed, when ϵ decreases for a fixed Ra , the ratio between the heating bottom surface and the cooling lateral surface also increases, leading to a larger global energy input into the system. We observe that a decrease in aspect ratio for a given Ra results in a greater horizontal temperature gradient (at least for non-turbulent flow). Consequently, this enhanced gradient drives a more substantial horizontal flow, leading to a larger U_{\max} .

We observe power-law behaviors for both T_{\max} and U_{\max} with exponents influenced by Ra . At lower Ra , we estimate the power exponents using the least squares method and find $U_{\max} \sim \epsilon^{-0.99 \pm 0.01}$ and $T_{\max} \sim \epsilon^{-1.99 \pm 0.02}$. To determine the mean exponent, we average the exponents, considering only data where $Ra \leq 3 \times 10^{-1}$ and for $\epsilon \leq 1/128$, with variability quantified by the largest difference between these exponents. At higher Ra , analyzing data where $Ra \geq 3 \times 10^{-1}$ and for $\epsilon \leq 1/128$, using a similar methodology, we find $U_{\max} \sim \epsilon^{-0.33 \pm 0.02}$ and $T_{\max} \sim \epsilon^{-1.35 \pm 0.02}$.

3.3. Theoretical analysis: Asymptotic bulk solution

Motivated by observations from Figure 3, we are interested in cases where the aspect ratio ϵ is small, i.e. a lubrication-type solution. Our first goal is to compute the 2D steady-state solution for the bulk, stable for a sufficiently small Rayleigh number. Let us detail the steady conservation equations that our analysis focuses on, which are also the equations solved by our BVP. For a system invariant along the y -direction, the steady dimensionless conservation equations of momentum, mass and energy in the x, z plane are

$$Pr^{-1}(UU_x + WU_z) = -P_x + U_{xx} + U_{zz}, \quad (3.1)$$

$$Pr^{-1}(UW_x + WW_z) = -P_z + RaT + W_{xx} + W_{zz}, \quad (3.2)$$

$$U_x + W_z = 0, \quad (3.3)$$

$$UT_x + WT_z = T_{xx} + T_{zz}. \quad (3.4)$$

We define the vertical average by

$$\bar{A}(x) \stackrel{\text{def}}{=} \int_0^1 A(x, z) \, dz. \quad (3.5)$$

Integrating the continuity equation (3.3) over the depth of the fluid gives the exact result $\bar{U}_x = 0$. With impenetrable sidewalls, this implies $\bar{U} = 0$. We introduce the

streamfunction ψ such that $(U, W) = (-\psi_z, \psi_x)$ and decompose the temperature field as

$$T = T^b(z) + \tilde{T}(x, z), \quad (3.6)$$

with

$$T^b(z) = f(\tfrac{1}{2}z^2 - \tfrac{1}{6}) - z + \tfrac{1}{2}. \quad (3.7)$$

The “boundary temperature” $T^b(z)$ is defined so that it satisfies the flux boundary conditions at $z = 0$ and 1 and has zero vertical average. Defining the rescaled horizontal coordinate $X = \epsilon x$, equations (3.1)–(3.4) reduce to

$$Pr^{-1}\epsilon\mathcal{J}(\psi, \epsilon^2\psi_{XX} + \psi_{zz}) = \epsilon Ra \tilde{T}_X + \epsilon^4\psi_{XXXX} + 2\epsilon\psi_{zzXX} + \psi_{zzzz}, \quad (3.8)$$

$$\epsilon\mathcal{J}(\psi, \tilde{T}) + \epsilon\psi_X T_z^b = \epsilon^2\tilde{T}_{XX} + \tilde{T}_{zz} + f, \quad (3.9)$$

where \mathcal{J} is the Jacobian operator $\mathcal{J}(A, B) = A_X B_z - A_z B_X$. The y -component of the vorticity is $-\epsilon^2\psi_{XX} - \psi_{zz}$. Figure 4 shows that in the diffusive regime ($Ra \ll 1$) the temperature scales as $T_{\max} \sim \epsilon^{-2}$. Thus we rescale the temperature by introducing rescaled temperature and Rayleigh numbers

$$\Theta = \epsilon^2 \tilde{T}, \quad \text{and} \quad \hat{Ra} = \epsilon^{-1} Ra. \quad (3.10)$$

These scalings are appropriate in the lubrication limit $\epsilon \rightarrow 0$ and are further justified below. With this notation equations (3.8)–(3.9) are

$$Pr^{-1}\epsilon\mathcal{J}(\psi, \epsilon^2\psi_{XX} + \psi_{zz}) = \hat{Ra} \Theta_X + \epsilon^4\psi_{XXXX} + 2\epsilon\psi_{XXzz} + \psi_{zzzz}, \quad (3.11)$$

$$\epsilon\mathcal{J}(\psi, \Theta) + \epsilon^3\psi_X T_z^b = \epsilon^2\Theta_{XX} + \Theta_{zz} + \epsilon^2 f. \quad (3.12)$$

Now integrate the energy equation (3.12) over depth. The boundary temperature $T^b(z)$ is defined so that the vertical average of Θ_{zz} is zero, and thus one factor of ϵ can be canceled from this vertical average. Then an integration in X produces

$$\overline{\psi\Theta_z} + \epsilon^2\overline{\psi T_z^b} + \epsilon\bar{\Theta}_X + \epsilon f X = 0. \quad (3.13)$$

In equation (3.13) the terms $\overline{\psi\Theta_z}$ and $\epsilon^2\overline{\psi T_z^b}$ are the advective heat transport, while $\epsilon\bar{\Theta}_X$ is the horizontal diffusion of heat; the last term, $\epsilon f X$, is the flux mismatch between the bottom and the top of the layer.

We seek a solution of (3.11) and (3.12) for the streamfunction and the rescaled temperature expanded in powers of ϵ as

$$\begin{aligned} \Theta(X, z) &= \Theta_0(X, z) + \epsilon\Theta_1(X, z) + \dots, \\ \psi(X, z) &= \psi_0(X, z) + \epsilon\psi_1(X, z) + \dots \end{aligned} \quad (3.14)$$

Substituting these expansions into (3.11) and (3.12) gives at the leading order

$$\Theta_{0zz} = 0, \quad \text{and} \quad \psi_{0zzzz} = -\hat{Ra}\Theta_{0X}. \quad (3.15)$$

The rescaled temperature has vertical boundary conditions $\Theta_z(X, 0) = \Theta_z(X, 1) = 0$. Thus the solution of the temperature equation in (3.15) is $\Theta_0 = \bar{\Theta}_0(X)$ i.e. the leading-order temperature is vertically uniform. We can then solve the vorticity equation in (3.15) to find

$$\psi_0 = \hat{Ra}P(z)G(x), \quad \text{where} \quad G = \bar{\Theta}_{0X}, \quad (3.16)$$

and

$$P(z) = -\frac{z^4}{24} + \frac{5z^3}{48} - \frac{z^2}{16}. \quad (3.17)$$

$P(z)$ is the polynomial equivalent to case c in [Chapman & Proctor \(1980\)](#). The temperature equation (3.12) at $O(\epsilon)$ is

$$\Theta_{1zz} = -\psi_{0z}G, \quad (3.18)$$

which integrates in z to

$$\Theta_{1z} = -\hat{Ra}P(z)G^2. \quad (3.19)$$

The construction above satisfies the boundary condition $\Theta_{1z} = 0$ at $z = 0$ and $z = 1$.

We do not need to compute explicitly ψ_1 to obtain G . Instead, consider the leading-order terms in the vertically averaged energy equation (3.13)

$$-\overline{\psi_0\Theta_{1z}} + G(1 - \epsilon\hat{Ra}\overline{PT_z^b}) + fX = O(\epsilon). \quad (3.20)$$

Using equation (3.15) and (3.19) to evaluate the vertical averages in (3.20) in terms of the master variable $G(x)$ we find

$$\alpha\hat{Ra}^2G^3 + \left(1 - \epsilon\hat{Ra}\frac{9-5f}{2880}\right)G + fX = O(\epsilon), \quad (3.21)$$

where

$$\alpha = \int_0^1 P(z)^2 dz = \frac{19}{1451520} \approx 1.3 \times 10^{-5}. \quad (3.22)$$

The G^3 -term in (3.21) results from $\psi_0 \propto G$ and $\Theta_{1z} \propto G^2$ in (3.20).

Below we proceed by discarding the $O(\epsilon)$ terms on the right of (3.21) and solving the resulting cubic equation for $G(X)$. We retain, however, the $O(\epsilon)$ term on the left of (3.21), i.e. we retain the term involving $(9-5f)/2880$ in the coefficient of G . This heuristic step produces a small but palpable improvement in agreement between the predictions of (3.21) and the numerical results reported in [Figure 6](#) and [Figure 7](#).

Exploratory calculations indicate that the $O(\epsilon)$ term on the left of (3.21) has a different and simpler physical character than other $O(\epsilon)$ terms resulting from complicated expressions for ψ_1 and Θ_2 . In particular, let $Ra_{cp}(f)$ denote the critical Rayleigh number of the Rayleigh-Bénard instability with flux mismatch f ; [Chapman & Proctor \(1980\)](#) study the special case $f = 0$. In [Appendix C](#) we generalize Chapman & Proctor's linear stability calculation to non-zero f and show that

$$Ra_{cp}(f) = \frac{2880}{9-5f}. \quad (3.23)$$

$f = 0$ recovers Chapman & Proctor's critical Rayleigh number 320. The $O(\epsilon)$ term on the left of (3.21) is therefore the ratio $Ra/Ra_{cp}(f)$.

3.4. Scaling

The isolation of two-term dominant balances in the cubic equation (3.21) helps us understand the scaling of velocity and temperature fields in low- and high- \hat{Ra} asymptotic regimes. With $\hat{Ra} \ll 1$ the cubic term $\alpha\hat{Ra}^2G^3$ can be neglected, leading to the balance $G \approx -fX$ (for scaling arguments we also neglect the order ϵ term). In this case the rescaled temperature profile that satisfies the side boundary condition ($\Theta_0 = 0$ at $X = 1$) is

$$\bar{\Theta}_0(X) \approx \frac{f}{2}(1 - X^2). \quad (3.24)$$

In this linear regime, diffusive processes dominate advection, and heat transport is mainly by diffusion. The $\hat{Ra} \ll 1$ scaling for the temperature and horizontal velocity fields is

$$\Theta \sim f, \quad \text{and} \quad U \sim \hat{Ra}f. \quad (3.25)$$

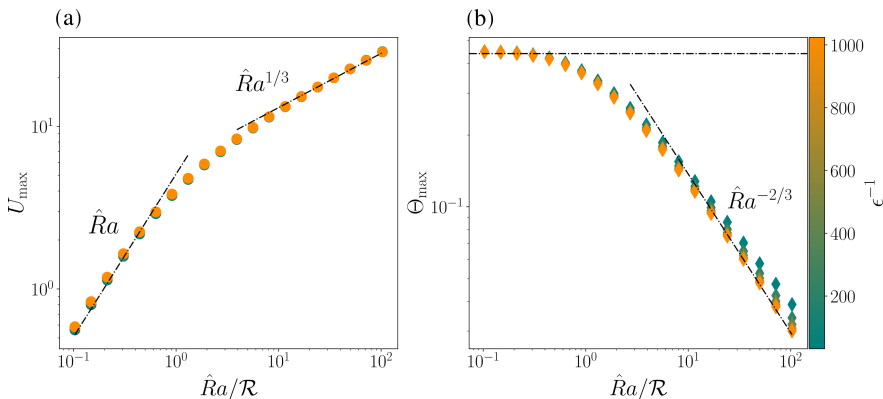


FIGURE 5. Peak values of (a) horizontal velocity, (b) rescaled maximal temperature $\Theta_{\max} = \epsilon^{-2}T_{\max}$ in the steady solution as a function of the rescaled Rayleigh number (\hat{Ra}) normalized by \mathcal{R} from (3.29) for several aspect ratios going from 1/1024 to 1/32. The BVP method is used to obtain the data, which corresponds to the simulations BVP1 to BVP6 listed in Table 1. The parameters are $Pr = 0.1$ and $f = 0.9$.

The rescaled temperature field is independent of \hat{Ra} and ϵ , while the horizontal velocity field is proportional to \hat{Ra} . These results match the scalings in Figure 4 where $T \sim \epsilon^{-2}\Theta \sim \epsilon^{-2}f$ and $U \sim Ra\epsilon^{-1}f$ (see (3.10)).

Now consider the asymptotic regime $\alpha\hat{Ra} \gg 1$. Then the G^3 term in (3.21) term dominates the middle term G , leading to the balance $G \approx -(fX/\alpha\hat{Ra}^2)^{1/3}$. In this case the rescaled temperature profile is

$$\bar{\Theta}_0(X) \approx \frac{3}{4}(f/\alpha\hat{Ra}^2)^{1/3} \left(1 - X^{4/3}\right). \quad (3.26)$$

In the $\alpha\hat{Ra} \gg 1$ regime, the scalings are

$$\Theta \sim \hat{Ra}^{-2/3}f^{1/3}, \quad \text{and} \quad U \sim \hat{Ra}^{1/3}f^{1/3}. \quad (3.27)$$

These results further support the scalings shown in Figure 4 as $T \sim Ra^{-2/3}\epsilon^{-4/3}$ and $U \sim Ra^{1/3}\epsilon^{-1/3}$.

At intermediate values of \hat{Ra} we are in the transition regime between (3.25) and (3.27) i.e. the three terms in the cubic (3.21) have the same order of magnitude

$$\alpha\hat{Ra}^2G^3 \sim G \sim f. \quad (3.28)$$

This three term balance implies that \hat{Ra} is approximately equal to the “regime transition Rayleigh number”

$$\mathcal{R} \stackrel{\text{def}}{=} \frac{1}{\sqrt{\alpha f}}. \quad (3.29)$$

Because $\alpha^{-1/2} \approx 276$, \mathcal{R} is significantly larger than f^{-1} . \mathcal{R} corresponds to the Rayleigh number at which the advective transport of heat flux can no longer be neglected compared to diffusion. With $\hat{Ra} \sim \mathcal{R}$ we expect to see a change in scaling behavior, which transitions from the low Rayleigh regime to the high Rayleigh regime. In Figure 5, we plot the data for the rescaled peak temperature and the horizontal peak velocity against \hat{Ra}/\mathcal{R} . At fixed f the renormalized Rayleigh number \hat{Ra}/\mathcal{R} is equivalent to dividing Ra by ϵ . We see in Figure 5 that with this normalization, the data sets for different aspect ratios collapse onto the same curve for both horizontal velocity (Figure 5(a)) and rescaled temperature data (Figure 5(b)). Figure 5 highlights the excellent agreement between the

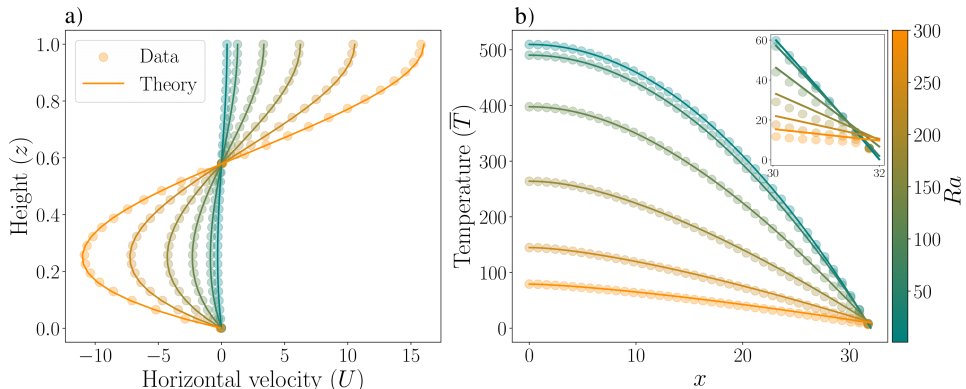


FIGURE 6. (a) Vertical profile of the horizontal velocity at $X = 2/3$, (b) Horizontal temperature profile ($\bar{T}(x)$) for Ra from 1 to 300. The inset shows a zoom of (b) in the $x \in [30; 32]$. Circles (\circ) represent numerical data from IVP method, listed as IVP4 to IVP9 in Table 1. Continuous lines are solutions of the cubic equation (3.21). The parameters are $\epsilon = 1/32$, $f = 0.9$ and $Pr = 0.1$.

theoretically predicted scalings in the low- and high-Rayleigh asymptotic regimes and the numerical data. The threshold at which the transition between these regimes occurs is consistent with the predictions from the scaling analysis: there is a break in slope when $\hat{Ra}/R \approx 1$. Figure 6 shows further excellent agreement between asymptotic solutions and numerical solutions. Figure 6a displays the vertical profile of horizontal velocity measured at $X = 2/3$, while Figure 6b shows the horizontal temperature profile for various values of Ra . The agreement between numerical and analytical solutions is robust across the entire Ra range. Discrepancies near the domain edges, corresponding to recirculation zones, highlight the limitations in the theoretical solution. These edge effects and the boundary conditions $T(X = \pm 1, z) = 0$ are not accounted for, becoming more pronounced as Ra increases. The recirculation area, localized within a characteristic size comparable to the domain height of order 1 in dimensionless units (see e.g. Figure 3), contributes to these discrepancies. In Figure 7, the horizontal velocity profile for $\epsilon = 1/512$, $Ra = 100$, $Pr = 0.1$, and $f = 1$ shows excellent agreement with the bulk solution up to $x = 510$ (Figure 7a). Figure 7b shows the velocity magnitude field in the (x, z) plane compared to the numerical data from IVP method and the analytical solution from (3.16). Discrepancies only emerge in the last two length units of the domain, coinciding with the recirculation zone.

In conclusion, the proposed analytical asymptotic solution exhibits very good agreement over a wide range of Ra values, covering a significant portion of the domain, particularly for small ϵ . In the following section, we investigate the instabilities present within the system.

4. Stability analysis

In this section, we highlight the onset of the instability observed in Rein *et al.* (2023, 2025) and perform both IVP simulations and Global-EVP analysis to characterize it. To understand the physical mechanisms behind this instability, we propose a reduced 1D model based on the analytical solution for the base state from the previous section. We perform a Local-EVP analysis on this reduced 1D model and characterize its stability. We then analyse the similarities between the instabilities in the reduced 1D model and the global instability, allowing us to draw conclusions on the physical mechanism responsible for the latter.

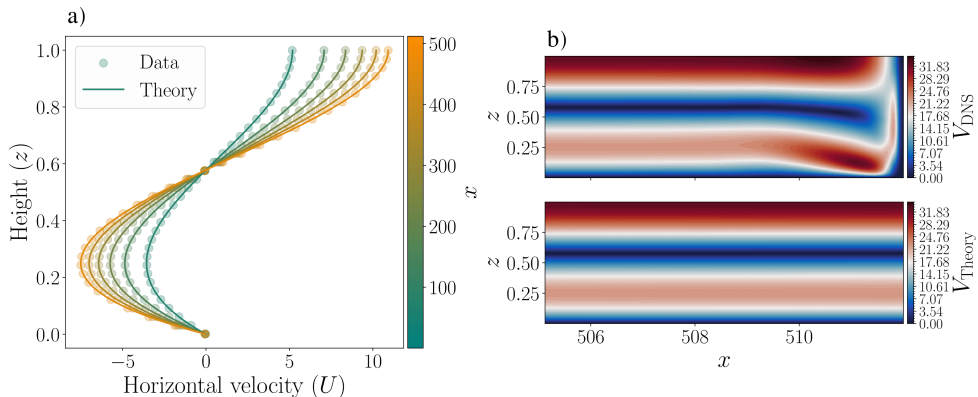


FIGURE 7. (a) Vertical profile of the base flow horizontal velocity (U) at several values of x from 0 to 510. Circles (\circ) represent numerical data from IVP method denoted IVP10 in Table 1, continuous lines are solutions from equation (3.16). (b) Velocity magnitude in the (x, z) plane: (top) numerical data from IVP10 (V_{DNS}) and (bottom) analytical solution from equation (3.16) (V_{Theory}).

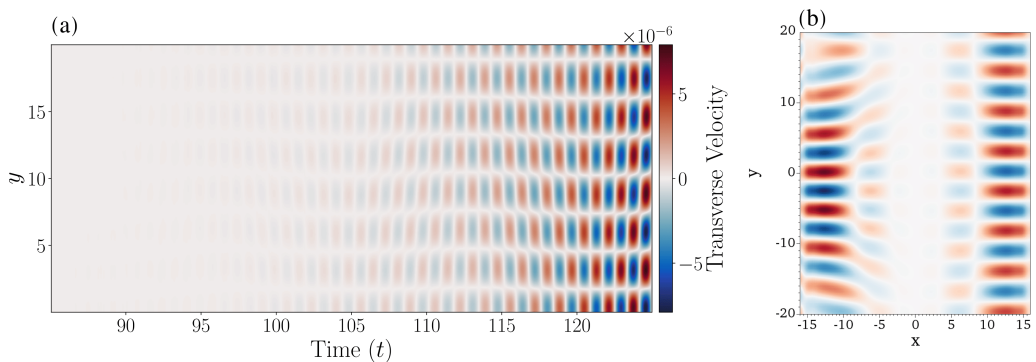


FIGURE 8. (a) Hovmöller (space-time) diagram of the z -averaged transverse velocity component (along the periodic y -direction) measured at $X = 3/4$. (b) 2D snapshot in the (x, y) -plane of the transverse velocity at $t = 120$. The IVP-DNS method is used to obtain the data and corresponds to the IVP11 simulation listed in Table 1. The parameters are $\epsilon = 1/16$, $L_y = 40$, $Pr = 0.1$, $f = 0.9$ and $Ra = 170$.

4.1. Phenomenology of the global instability

Using IVP simulations from Nek5000 and Global-EVP from Dedalus, we characterize the first instability identified in the system. We focus on identifying thresholds for different aspect ratio, normalized flux difference and Prandtl number, and evaluate the variation of the transverse wave number as well as angular frequency as a function of the input parameters.

4.1.1. DNS analysis

We start the analysis by showing the transient dynamics of this system at a low value of $Ra_\phi = 170$ (well below the typical values considered in Rein *et al.* (2023, 2025)) In Figure 8, we present a Hovmöller diagram showing the space-time evolution of the z -averaged transverse velocity (v), measured at $X = 3/4$. Figure 8 reveals the emergence of a three-dimensional instability near the sidewalls. For the given parameters, this instability occurs at a Ra value well below the Chapman & Proctor purely thermal instability threshold of 640 (for $f = 0.9$, see Appendix C). The insets show that the

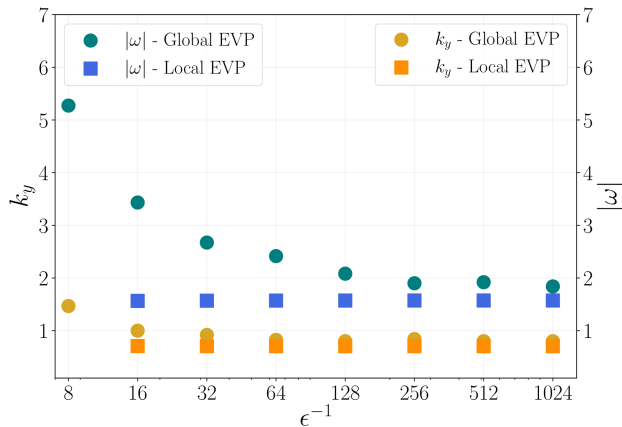


FIGURE 9. Angular frequency $|\omega|$ and transverse wavenumber k_y as functions of ϵ for both Global and Local EVP analysis. For each method Ra is set to the threshold value identified for each aspect ratio. The Global-EVP method is used to obtain the data corresponding to simulations GEVP1 to GEVP5 and GEVP9 and the Local-EVP method is used to obtain the data corresponding to simulations LEVP1 to LEVP9 as listed in Table 1. For both, $f = 0.9$ and $Pr = 0.1$.

instability is characterized by a transverse y -wavelength approximately seven times the layer height, a vertical wavelength equal to the layer height, and a horizontal structure extending six times the layer height in the x -direction, from the sides. This horizontal structure decays as it moves toward the centre. Two standing waves, positioned near each boundary in the x -direction and oscillating in antiphase, are observed. Notice that an oscillating pattern is characteristic of convective instability at low Prandtl number (Busse 1972; Clever & Busse 1990).

4.1.2. Global EVP analysis

We now use a global eigenvalue analysis to characterize the properties of the global instability observed at low Ra and low Pr . Figure 9 shows the variation with ϵ of $|\omega|$ and k_y of the first unstable mode at the critical value of Ra . The angular frequency ω is defined as the imaginary part of the complex growth rate σ . Each plot focuses on the mode with the highest growth rate, measuring its transverse wavenumber and angular frequency. In Figure 9, ϵ changes while Ra is fixed at the critical value for each aspect ratio. At the onset of instability, as the aspect ratio decreases, the values of k_y and ω tend to constant values, becoming independent of the aspect ratio. This behaviour shows that the underlying physical mechanism driving the instability is local.

Next, we analyse the effect of the Prandtl number on the system stability. To do so, we consider the case $\epsilon = 1/32$ and $f = 0.9$. For each Prandtl number from 0.1 to 0.4, we determine the critical Rayleigh number. Figure 10(a) shows the critical Rayleigh number as a function of Pr . We observe that increasing the Prandtl number has a stabilizing effect consistent with the qualitative observations in Figure 18 (see Appendix C.2), where the system remains stable for $Pr = 1$ even at Rayleigh numbers exceeding the Chapman & Proctor instability threshold. The larger the Prandtl number the larger the threshold. A slight change in behaviour can be noted when $Pr \simeq 0.23$. In Figure 10(b) we plot the eigenmode structure in a 2D (x, z) plane of the perturbation of the transverse velocity for several Prandtl values at $Ra = Ra_c$. We observe an expanding structure of the mode in the x -direction when Pr increases, until it covers the entire domain for $Pr = 0.3$. Close to

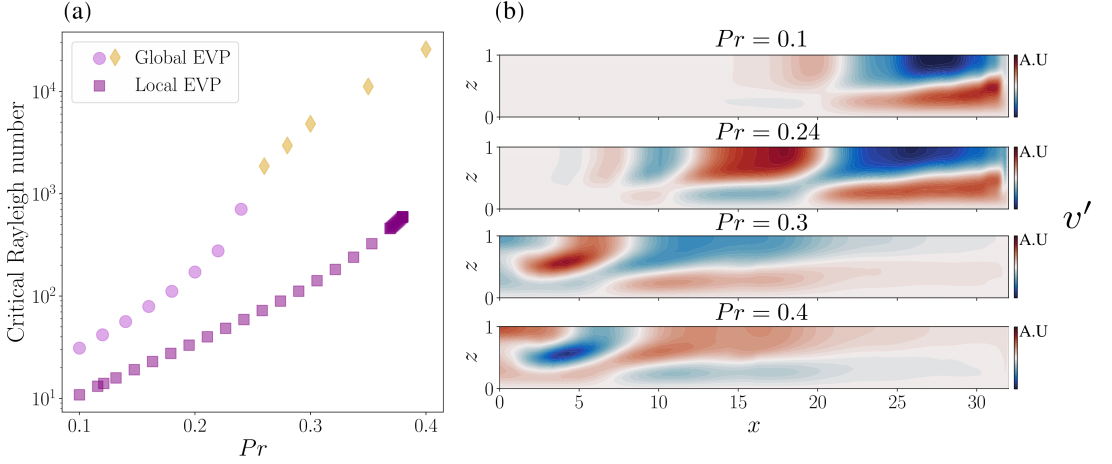


FIGURE 10. (a) Critical Rayleigh number (Ra_c) as a function of the Prandtl number using both Global and Local EVP analysis. For all data, the critical wavenumber $k_y = 0.92$ (\circ and \square) except when $Pr \geq 0.26$ where $k_y = 0.58$ (\diamond). (b) Perturbed transverse velocity for various Prandtl numbers from 0.1 at the top to 0.4 at the bottom at $Ra = Ra_c$. The colorbars are centered around zero, with white indicating zero values. Positive values are shown in red and negative values in blue. The Global-EVP method is used to obtain the data corresponding to simulations GEVP10 to GEVP16, as listed in Table 1.

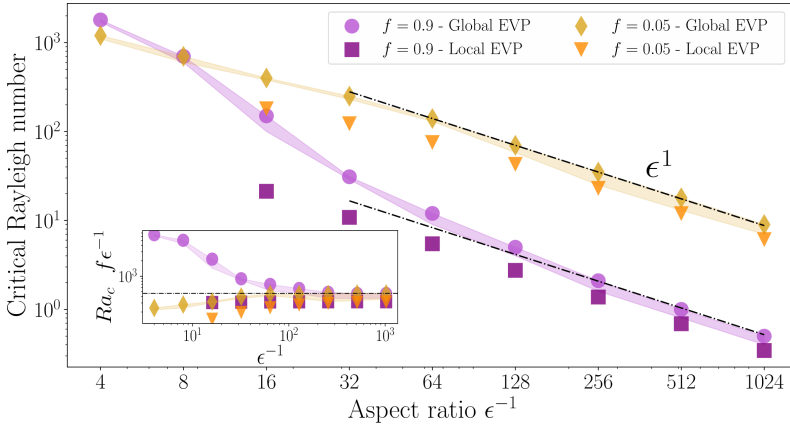


FIGURE 11. Critical Rayleigh number Ra_c as a function of aspect ratio for $f = 0.05$ and $f = 0.9$ for both Global and Local EVP analysis. The dash-dotted lines indicate the best fit following a ϵ^{-1} law. The inset shows the compensated critical Rayleigh number. The horizontal dash-dotted line is set at 462. The Global-EVP method is used to obtain the data corresponding to simulations GEVP1 to GEVP8, as listed in Table 1. Data for $\epsilon = 1/4$ are obtained using IVP-DNS simulation denoted IVP12. For all, $Pr = 0.1$.

the side, the structure of the mode changes when $Pr \approx 0.24$, corresponding to the slight change in behaviour of Ra_c observed in Figure 10(b). The same expanding behaviour happens for all the other perturbation variables. For $Pr < 0.24$, we find the same wave number $k_y = 0.92$ associated with the most unstable mode. However, when $Pr > 0.24$ a different modal structure, mainly located at the center of the domain, is observed. The critical wavenumber is found to be $k_y = 0.58$. The primary global instability mode, identified at low Prandtl number, disappears between $0.2 < Pr < 0.3$, leading to another instability with much higher threshold.

To determine how the critical Rayleigh number (Ra_c) depends on the parameters, we conducted a stability analysis using the Global-EVP method. Beginning with a starting Ra value, we varied k_y from 10^{-2} to 5×10^1 . Employing a bisection method on Ra , we look for the first Ra for all k_y having a zero real part of the growth rate. This method enabled us to approach the critical Ra as a function of ϵ and Pr . Figure 11 shows that for $f = 0.05$ and $f = 0.9$, as ϵ decreases, the instability threshold decreases. Configurations with larger normalized flux differences are more unstable compared to those with lower normalized flux differences. For both normalized flux difference regimes, a power law behaviour is noted, with a +1 exponent for the aspect ratio dependency. The asymptotic behaviour is obtained at lower aspect ratio when f is low. For $f = 0.05$ the asymptotic behaviour starts at $\epsilon \simeq 1/64$, while we need to reach $\epsilon \simeq 1/256$ for $f = 0.9$. In the inset, we plot the critical Rayleigh number compensated by $f\epsilon^{-1}$. All the data collapse onto the same straight line indicating a universal law related to the global instability. In the next section, we focus on identifying the physical mechanism underlying the global instability.

4.2. Local analysis

We have identified the characteristics of the instability as being three-dimensional, oscillatory, and emerging near the edge of the domain for low enough Prandtl number. To capture the physical mechanism responsible for this phenomenon, we study a simplified version of the problem.

4.2.1. Reduced 1D model: dominant terms of the base state

To build a relevant reduced model, we aim to study the stability of the flow in the bulk of the system, without considering the impact of the sidewall. To describe it, we use the steady-state analytical asymptotic solution of the base state detailed in subsection 3.3. We want to simplify the flow description by keeping only the dominant contributions. We compute the horizontal temperature gradient $T_X = \epsilon^{-2}\Theta_{0X} = \epsilon^{-2}G(x)$ using the leading-order rescaled temperature solution, solving the cubic equation (3.21). Velocities are computed from the streamfunction relation (3.16) at the leading order and the vertical temperature gradient is computed using the $O(\epsilon)$ solution of the rescaled temperature thought the relationship

$$T_z = T_z^b(z) + \epsilon^{-1}\Theta_{1z} = fz - 1 - \epsilon^{-1}\hat{Ra}P(z)G^2(x). \quad (4.1)$$

The mass conservation equation (3.3) implies that the vertical velocity is smaller by a factor of ϵ than the horizontal velocity. Therefore, only the horizontal velocity is considered in describing the base flow. We finally obtain a simplified base state description characterized by $\mathbf{U} = (U(z), 0, 0)$ with a vertical shear U_z as well as horizontal T_x and vertical T_z temperature gradients (see Figure 12). As suggested by the location of the unstable mode in Figure 8, we perform a local analysis of the base state at $x = \epsilon^{-1}$. This position coincides with the location where both velocity and thermal gradients are the strongest.

4.2.2. Local EVP analysis

We now perform a numerical eigenvalue analysis of the reduced 1D model, using the Local-EVP method described in §B.1.2 solving the equations (B 14)–(B 18) with the boundary conditions (B 6). Note that contrary to the global EVP approach used above, which was homogeneous in y only, the local EVP is homogeneous in both x and y -directions.

The Local-EVP simulation listed in LEVP7 in Table 1 is performed for the case $x = 1/128$, $Pr = 0.1$, $f = 0.9$ at just above the onset ($\sigma \gtrsim 0$) for $Ra = 2.75$.

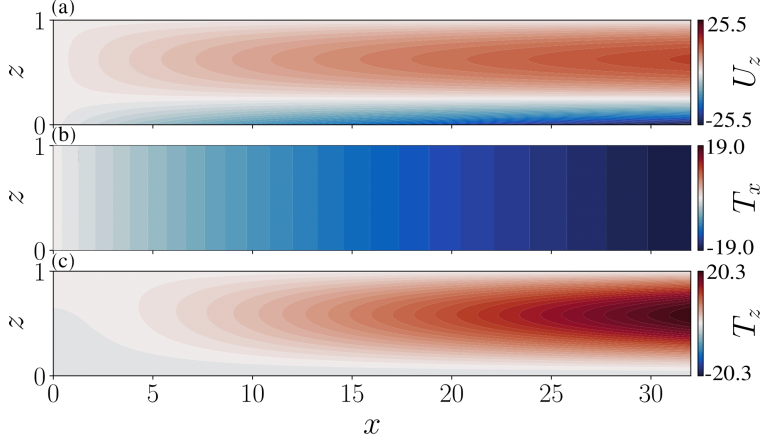


FIGURE 12. Simplified base state from the analytical solution (3.16), (3.19), (3.21). (a) Vertical shear (U_z), (b) horizontal and (c) vertical temperature gradient. The parameters are $Pr = 0.1$, $f = 0.9$, $Ra = 10.84$ and $\epsilon^{-1} = 32$.

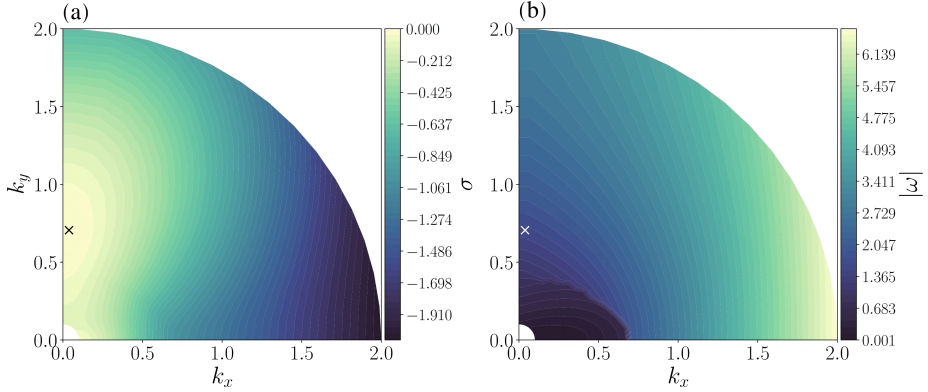


FIGURE 13. (a) Real part of the growth rate and (b) absolute value of the angular frequency in a (k_x, k_y) map. The cross indicates the location of the maximal growth rate.

Figure 13 displays the growth rate and angular frequency in (k_x, k_y) space for these parameters. We observe a positive growth rate with the most unstable mode exhibiting transverse oscillations characterized by $k_y = 7.0 \times 10^{-1}$, $k_x = 1.93 \times 10^{-2}$, and $\omega = 1.57$. For $\epsilon = 1/128$, the global instability is characterized by $Ra_c = 5.0$ with $k_y = 0.85$, $\omega = 2.08$ for the most unstable mode. These values are similar in magnitude to the results obtained from the Local-EVP method. Despite the difference between the local ($Ra_c = 2.75$) and global ($Ra_c = 5.0$) thresholds, both remain significantly lower than the Chapman–Proctor threshold ($Ra_{cp} = 640$). The local analysis shows an oscillating 3D instability for the most unstable mode, but it is associated with $k_x \simeq 0$, revealing a limitation of our local approach. In Figure 9, we present the values of $|\omega|$ and k_y associated with the most unstable mode predicted by the local model, plotted as functions of ϵ . Across all aspect ratios, the local analysis consistently yields $|\omega| = 1.57$ and $k_y = 0.70$. As the aspect ratio decreases, the global analysis results for $|\omega|$ and k_y converge toward these similar constant values obtained from the local model. The lower the aspect ratio, the better the agreement between the global and local analysis.

We now compare the vertical eigenmode structure for the most unstable mode from the Local-EVP analysis and from the Global-EVP analysis for the case $\epsilon = 1/128$, $Pr = 0.1$,

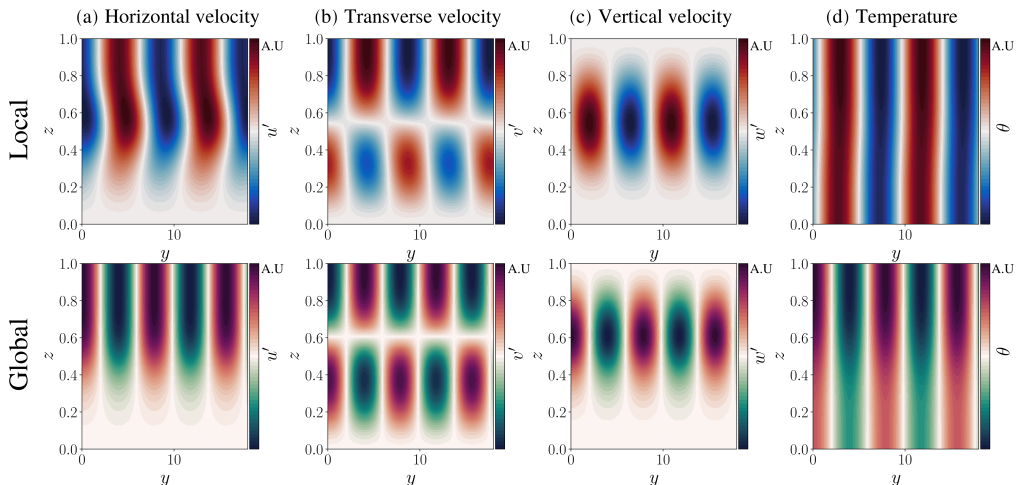


FIGURE 14. Eigenmode maps in a (y, z) plane of the (a) horizontal velocity, (b) transverse velocity, (c) vertical velocity and (d) temperature. The top row shows eigenmodes from local EVP computations, while the bottom row displays global EVP computations. The global eigenmodes are for $Ra = 5.0$, $\epsilon = 1/128$ at $x = 126$ with $k_y = 0.85$ and the local eigenmodes are for $Ra = 2.75$, $\epsilon = 1/128$ at $x = 128$ with $k_y = 0.70$ and $k_x = 1.93 \times 10^{-2}$. The colorbars are centered around zero, with white indicating zero values. Positive values are shown in red and negative values in blue. Data correspond respectively to LEVP7 and GEVP5 simulations listed in Table 1.

$f = 0.9$ and $Ra = Ra_c$ ($Ra_c = 2.75$ and 5.0 for the local and global analysis, respectively). Figure 14 illustrates the perturbation velocity and temperature fields maps in (y, z) plane for the most unstable mode, taken at $x = 126$ and 128 for the global and local analysis, respectively. We choose to look at the global mode structure at $x = 126$ to avoid the influence of the recirculation flow near the edge. There is a strong similarity in the vertical mode structure between the local and global approaches for all perturbation fields.

With this local approach, we investigate the Prandtl number dependence by solving Local-EVP at $x = 32$, $f = 0.9$, seeking the critical Rayleigh number for each Prandtl number value going from 0.1 to 0.38 . In Figure 10(a), we notice the same stabilizing effect for larger Pr as that identified in the global analysis: the larger Pr , the larger the threshold. It should be noted that the most unstable mode reaches an asymptotic value $Pr \simeq 0.38$ and then disappears (i.e. a mode with a completely different structure, present but subcritical before, now becomes the most unstable one). This behaviour is consistent with the changing mode structure identified for $Pr \approx 0.24$ from the global analysis. This transition in mode structure also explains why, at larger Prandtl numbers (e.g. $Pr = 0.3$), the critical Rayleigh number from the global EVP is about an order of magnitude larger than that from the local analysis, since the instability is then governed by global rather than local dynamics (see Figure 10(b)).

Finally, we compute the marginal stability curve related to the local model, i.e. the critical Rayleigh number as a function of the aspect ratio. The results are plotted in Figure 11 and show thresholds lower than those for the global approach. This difference tends to decrease as the aspect ratio decreases but a slight difference persists for very low aspect ratio, e.g. $Rac = 0.34$ and 0.5 at $\epsilon = 1/1024$, $f = 0.9$ for the local and global analysis respectively. It should be noted, however, that the same universal ϵf^{-1} power law behaviour is identified (see insert from Figure 11).

This analysis emphasizes that such a base state, resulting from a bottom/top flux

mismatch leading to vertical shear combined with horizontal and vertical temperature gradients, significantly lowers the stability threshold compared to the purely thermal threshold of Chapman & Proctor. The threshold value for purely thermal instability at $f = 0.9$ is 640, and it remains independent of the aspect ratio. In contrast, the threshold found from local analysis under the same conditions decreases as the aspect ratio decreases, following a ϵf^{-1} power law and reaching a value of 0.35 for $\epsilon = 1/1024$. Similar behaviour was identified for the low- Pr regime by [Ortiz-Pérez & Dávalos-Orozco \(2014, 2015\)](#); [Patne & Oron \(2022\)](#) in the context of an inclined thermal gradient where both horizontal and vertical gradients of temperature are fixed. In our system, the horizontal temperature gradient is a dynamic consequence of the difference in flux between the top and bottom.

The local analysis of the reduced 1D model identifies a 3D oscillatory instability in the low Ra regime. Despite the limitations of the local approach, in particular accounting for the fact that the most unstable mode has $k_x \simeq 0$, it exhibits strong similarities to the global instability. In the asymptotic limit of small aspect ratios, the transverse wavenumber and angular frequency converge to similar constant values, with perturbation fields displaying a similar vertical mode structure. The dependence on the Prandtl number is also consistent between the two approaches, showing a stabilizing effect as Pr increases and the disappearance of the most unstable mode around $Pr \simeq 0.3$. Furthermore, both local and global analyses reveal the same asymptotic behavior for small aspect ratios, where the critical Rayleigh number follows a ϵf^{-1} power law. These shared characteristics confirm the relevance of the local model in capturing key features of the global instability. Given its ability to reproduce many aspects of the global instability, we now leverage the analytical results of the local analysis to further investigate the underlying instability mechanisms.

4.2.3. Instability mechanisms

In this section, we analyze the linear perturbation equations (B 14)–(B 18) given in Appendix B.1.2, further assuming a Fourier decomposition in the z -direction. Performing the necessary algebraic manipulations, we obtain the following cubic dispersion relation

$$\lambda^3 - \lambda^2(\mathcal{S} - \mathcal{D}) + \lambda(\mathcal{C} - \mathcal{SD}) - \mathcal{B} = 0, \quad (4.2)$$

where

$$\begin{aligned} \mathcal{S} &= U_z q_x q_z, & \mathcal{C} &= RaPr [T_z(1 - q_z^2) - T_x q_x q_z], \\ \mathcal{D} &= k^2(1 - Pr), & \mathcal{B} &= RaPr U_z T_x q_y^2, \end{aligned} \quad (4.3)$$

and $\lambda = \sigma + Prk^2 + i(Uk_x + \omega)$ with $q_j = k_j/k$ for $j = x, y, z$ and $k^2 = k_x^2 + k_y^2 + k_z^2$. Although the Fourier decomposition in the z -direction is an approximation due to the top/bottom boundary conditions, this local analysis remains valuable for identifying the dominant instability mechanisms. The dispersion relation (4.2) reveals four distinct contributions:

(i) A shear term \mathcal{S} , proportional to the vertical velocity gradient U_z , representing a potential source for the shear instability. This term contributes to 2D disturbances in the (x, z) plane.

(ii) A diffusive term \mathcal{D} , arising from the disparity between viscous and thermal diffusion. This contribution is spatially uniform and changes sign depending on whether the Prandtl number is greater or less than one.

(iii) A convective term \mathcal{C} , that includes the effects of the background temperature gradients and composed of two parts. The first part reflects the influence of the vertical temperature gradient in the base state: it is stabilizing when $T_z > 0$ (i.e. stably stratified)

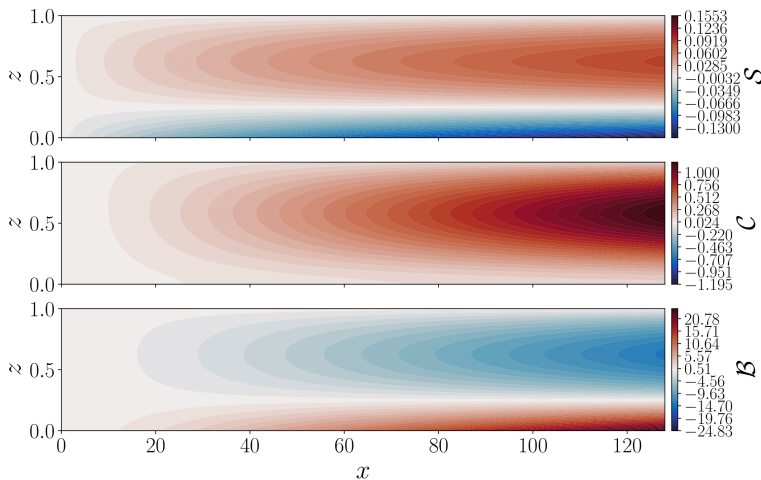


FIGURE 15. Maps in the (x, z) plane of the shear term \mathcal{S} (top), the convective term \mathcal{C} (middle) and the baroclinic term \mathcal{B} (bottom) for the case $\epsilon = 1/128$, $f = 0.9$, $Pr = 0.1$ and $Ra = 2.75$, corresponding to the threshold value identified from the local EVP analysis. $k_x = 1.93 \times 10^{-2}$, $k_y = 0.70$, corresponding to the most unstable mode from the local EVP while $k_z = \pi$. The diffusive term is uniform across the domain with a constant value $\mathcal{D} = 9.32$.

and destabilizing when $T_z < 0$, as in the classical Rayleigh–Bénard configuration. Based on the base state shown in Figure 12, this term is destabilizing near the center and bottom of the domain, where $T_z < 0$ due to the imposed heat flux at the lower boundary. In contrast, further from the center and in the bulk of the domain, the term becomes stabilizing ($T_z > 0$), due to re-stratification induced by horizontal advective heat transport. This effect is captured by the term $-\epsilon^{-1} \hat{R}a P(z) G^2(x)$ in equation (4.1) where $P(z) < 0$ for all $z \in [0, 1]$. Such restratification has also been observed by Patne & Oron (2022); Dixit *et al.* (2024) in configurations with imposed oblique temperature gradients.

The second part of the convective term \mathcal{C} involves the horizontal temperature gradient T_x which is negative throughout the domain. This contribution is stabilizing for perturbations with $q_x, q_z > 0$, and does not lead to disturbances in the y -direction.

(iv) A baroclinic term \mathcal{B} , representing the interaction between vertical shear and horizontal temperature gradient. It is proportional to the product $U_z T_x$, and its effect depends on the sign of this product (i.e. the sign of U_z since $T_x < 0$ throughout the domain). Moreover, this is the only term that exclusively affects transverse modes ($k_y \neq 0$).

The key elements associated with this mechanism are U_z and T_x . This coupling bears some similarities to baroclinic instability, which also relies on the interaction between vertical shear and horizontal temperature gradient. Classical baroclinic instability, however, is derived in rotating systems, where the base flow is in thermal wind and geostrophic balance (e.g. Pedlosky 2013). This fundamental aspect sets baroclinic instability apart from our case. In our configuration, there is no background rotation and no geostrophic balance. While our base state does feature vertical shear and horizontal temperature gradient, the nature of their interaction differs from that of baroclinic instability: the vertical shear U_z is aligned with the horizontal temperature gradient T_x , whereas in baroclinic instability the vertical shear is perpendicular to the thermal gradient.

Figure 15 shows maps of \mathcal{S} , \mathcal{C} , and \mathcal{B} for an unstable case identified via the local EVP analysis, slightly above the onset. Here k_x and k_y are the wavenumbers of the most unstable local mode, while $k_z = \pi$. The diffusive term $\mathcal{D} = 9.32$ is uniform throughout the domain. Slightly above onset, the relative magnitudes are $\|\mathcal{B}\| \gg \|\mathcal{D}\| \gg \|\mathcal{C}\| \gg \|\mathcal{S}\|$, suggesting a dominant balance $\lambda^3 \approx \mathcal{B}$ from the dispersion relation (4.2).

Since the instability is oscillatory, it is expected to arise in regions where $\mathcal{B} < 0$, typically near the side in the upper half of the domain (see the bottom panel of Figure 13). In this area, the dispersion relation yields a pair of complex-conjugate eigenvalues with positive real parts. Consequently, the approximate real part of the growth rate is

$$\sigma \approx |RaPrU_zT_xq_y^2|^{1/3} - Prk^2. \quad (4.4)$$

To estimate the critical Rayleigh number at the onset ($\sigma = 0$), we use scalings derived from the bulk base-state solution in §3, valid in the asymptotic regime $\epsilon \ll 1$ with $Ra \sim O(1)$. In this regime, the vertical shear and horizontal temperature gradient scale as

$$U_z \sim \hat{Ra}P'\Theta_{0X} \sim Ra f \epsilon^{-1} \quad \text{and} \quad T_x \sim \epsilon^{-2}\Theta_{0x} \sim f \epsilon^{-1}. \quad (4.5)$$

Substituting relation (4.5) into (4.4) gives the scaling

$$Ra_c \approx \frac{\epsilon Pr}{f}. \quad (4.6)$$

This scaling is consistent with the trend observed in Figure 11, confirming that $Ra_c \sim \epsilon f^{-1}$. Equation (4.6) further indicates that the larger Pr the more stable the system, as observed in both global and local analyses. Physically, the stabilizing effect of the Prandtl number can be interpreted as arising from viscous damping of the perturbation and from the decrease of the vertical shear amplitude, which reduces the destabilizing forcing. Altogether, these findings suggest that the instability is driven by a baroclinic-type mechanism, resulting from the interaction between the vertical shear and the horizontal temperature gradient.

However, our analysis has not accounted for the effects of the domain edge. It is plausible that the localized recirculation near the side could stabilize the instability described here, as this recirculation alters the flow profile and the no-slip condition at the side results in increased viscous dissipation. This phenomenon may explain why the critical Rayleigh number is smaller in the local approach than in the global one. Nevertheless, we cannot rule out the possibility that this recirculation is also contributing to the observed instability. Streamline curvature, which increases with lower ϵ , combined with the horizontal temperature gradient, may induce a thermo-centrifugal type 3D instability. Mutabazi & Bahloul (2002); Yoshikawa *et al.* (2013); Meyer & Mutabazi (2015) studied such coupling extensively in the context of a canonical Taylor-Couette flow subjected to a fixed radial temperature gradient. Further analysis is needed to fully understand this additional effect in the global system, which we leave for future studies.

5. Conclusion

In this study, we analysed the flow structure for small aspect ratios of a thin fluid layer with imposed heat flux at the top and bottom and imposed temperature at the side. Near the edge, a vortex recirculation zone was identified, whose characteristic size is independent of the aspect ratio. We described the bulk base state using an asymptotic approach based on lubrication theory, which accurately captures the vertical and horizontal structures of the velocity and temperature fields in the small aspect ratio

regime. The bulk solution shows some expected differences only in the vortex region near the sidewall.

A detailed characterization of system instability revealed that the most unstable mode is three-dimensional, featuring two superimposed oscillatory standing waves in the transverse direction close to the domain edge. During the exponential growth phase of the instability, these waves interact non-linearly, ultimately producing a drift pattern as illustrated in Figure 16. A preferred drift direction is selected, either forward or backward (clockwise or counterclockwise in cylindrical geometry), consistent with the findings of Rein *et al.* (2023). A weakly non-linear study is necessary in order to understand the mechanism at the origin of the drift. The instability threshold decreases with the normalized flux difference and increases with aspect ratio, following a $f^{-1}\epsilon$ power law behaviour. We found that increasing the Prandtl number stabilizes the system and spreads out the mode structure localised near the edge to the bulk without changing the transverse wavenumber. For $Pr \simeq 0.3$ a complete change in modal structure is identified, the transverse wavenumber changes and the mode structure becomes localised around the center.

We proposed a 1D reduced model based on the analytical solution for the bulk base state in order to simplify the system and capture the physical mechanisms responsible for the global instability. We performed a local stability analysis of this model and showed oscillating transverse instabilities for unexpectedly low Rayleigh thresholds. However, we also found instability for horizontal wavelengths similar to the domain size, challenging our local analysis assumption.

Despite the limitations of the local approach it exhibits strong similarities with the global instability. In the asymptotic limit of small aspect ratios, the transverse wavenumber and angular frequency converge to similar constant values, with perturbation fields displaying a similar vertical mode structure. The dependence on the Prandtl number is also consistent between the two approaches, showing a stabilizing effect as Pr increases and the disappearance of the mode around $Pr \simeq 0.3$. Furthermore, both local and global analyses reveal the same asymptotic behavior for small aspect ratios, where the critical Rayleigh number follows a ϵf^{-1} power law. These shared characteristics confirm the relevance of the local model in capturing key features of the global instability.

In our local analysis, we identified three mechanisms contributing to instability: a vertical shear, a Rayleigh-Bénard-type thermal forcing, and a third mechanism arising from the coupling between vertical shear and horizontal temperature gradient, reminiscent of baroclinic-type instabilities. By solving the perturbation equations in Fourier modes, we showed that this coupling produces the same ϵf^{-1} scaling law for the critical Rayleigh number and it also captures the stabilizing effect of increasing the Prandtl number. Although all mechanisms give rise to identifiable modes in the stability analysis, the baroclinic-type mechanism is the most unstable with surprisingly low critical Rayleigh number threshold, and is thus most likely responsible for the dominant unstable mode observed at low Prandtl numbers in the DNS.

To return to the nuclear context motivating this study, the patterns observed here persist into the turbulent regime (Rein *et al.* 2023). Rein *et al.* (2025) showed experimentally in cylindrical geometry that drifting patterns are responsible for transporting a significant fraction of the heat flux along the sidewalls, thereby contributing to localized abrasion of the vessel wall. The present analysis provides new insight into the physical mechanisms underlying the patterns' emergence, which may inform future suppression or control strategies. An interesting implication of these results is that modifying the composition of the metallic layer, and therefore its effective Prandtl number, could alter the structure of the unstable modes and consequently modify the drifting pattern and

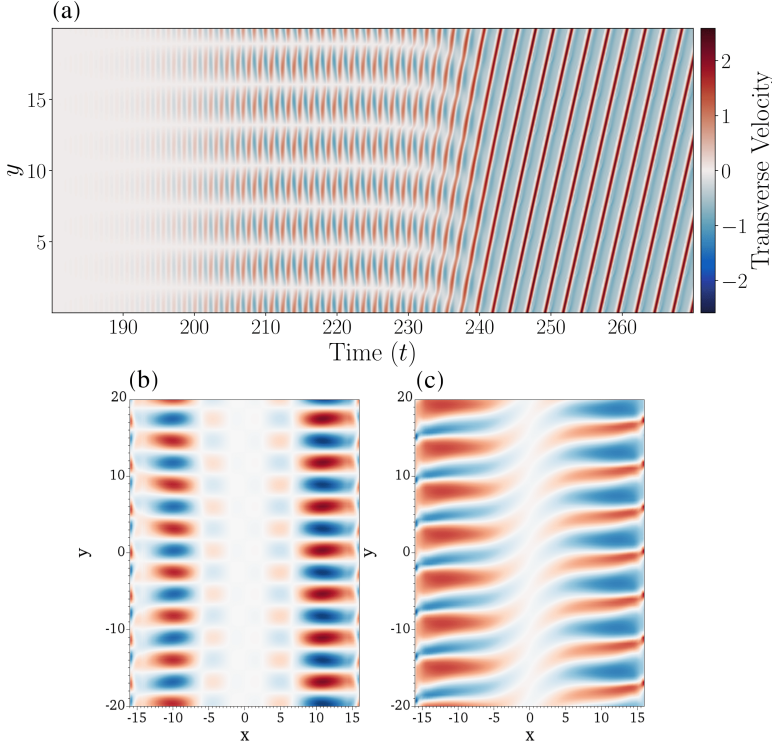


FIGURE 16. (a) Hovmöller(space-time) diagram of the z -averaged transverse velocity measured at $X = 3/4$. 2D snapshots in the (x, y) -plan of the transverse velocity at (b) $t = 210$ and (c) $t = 260$. The IVP-DNS method is used to obtain the data which correspond to the simulation IVP11 listed in Table 1. The parameters are $\epsilon = 1/16$, $L_y = 40$, $Pr = 0.1$, $f = 0.9$ and $Ra = 170$.

sidewall transport. While this points to a possible route for mitigating wall-localized fluxes, any practical application would be subject to significant material, structural and safety constraints, and lies beyond the scope of the present study.

Acknowledgements

This work was supported by the Institut de Radioprotection et de Sûreté Nucléaire (IRSN), the Commissariat à l'Énergie Atomique et aux Énergies Alternatives (CEA), Électricité de France (EDF), and the Simons Foundation. Centre de Calcul Intensif d'Aix-Marseille is acknowledged for granting access to its high performance computing resources. This work was granted access to the HPC resources of IDRIS under the allocation 2025-A0180407543 made by GENCI. FR, BF and MLB would like to thank Florian Fichot, Laure Carenini and Jean-Marc Ricaud from the Nuclear Safety and Radiation Protection Authority for bringing this problem to their attention and for further fruitful discussions.

Declaration of Interests

The authors declare no competing interests. The funding organizations—IRSN, CEA, EDF, and the Simons Foundation—had no involvement in the study design, data collection, analysis, interpretation, or the decision to publish. Responsibility for the content lies solely with the authors.

Appendix A. Summary of the simulation parameters

Table 1 provide all relevant parameters for the simulations performed using the IVP, BVP, Global-EVP and Local-EVP approaches.

Appendix B. Numerical methods

B.1. Eigenvalue analysis

To carry out an eigenvalue analysis, we consider the background state, invariant in the y -direction, with a pressure and temperature profile denoted $P(x, z)$ and $T(x, z)$ and with a 2D base flow $\mathbf{U} = (U(x, z), 0, W(x, z))$. This base state can come from analytical considerations or from solving BVP, as shown below. We then consider perturbations to the base state with pressure and temperature perturbations denoted $p'(x, y, z)$ and $\theta(x, y, z)$ and with a perturbation flow $\mathbf{u}' = (u'(x, y, z), v'(x, y, z), w'(x, y, z))$.

The linearized conservation equations of momentum, mass and energy become

$$u'_t + (\mathbf{U} \cdot \nabla) u' + (\mathbf{u}' \cdot \nabla) U = -p'_x + Pr \nabla^2 u', \quad (\text{B1})$$

$$v'_t + (\mathbf{U} \cdot \nabla) v' = -p'_y + Pr \nabla^2 v', \quad (\text{B2})$$

$$w'_t + (\mathbf{U} \cdot \nabla) w' + (\mathbf{u}' \cdot \nabla) W = -p'_z + RaPr\theta + Pr \nabla^2 w', \quad (\text{B3})$$

$$u'_x + v'_y + w'_z = 0, \quad (\text{B4})$$

$$\theta_t + (\mathbf{U} \cdot \nabla) \theta + (\mathbf{u}' \cdot \nabla) T = \nabla^2 \theta, \quad (\text{B5})$$

with the boundary conditions

$$\begin{aligned} \mathbf{u}' &= \mathbf{0} \quad \text{and} \quad \theta_z = 0 \quad \text{at} \quad z = 0, \\ u'_z = v'_z = w'_z &= 0 \quad \text{and} \quad \theta_z = 0 \quad \text{at} \quad z = 1, \\ \mathbf{u}' &= \mathbf{0} \quad \text{and} \quad \theta = 0 \quad \text{at} \quad x = \epsilon^{-1}. \end{aligned} \quad (\text{B6})$$

This problem leads to two types of eigenvalue problems depending on the base state. A Global Eigenvalue Problem, denoted *Global EVP*, which involves a two-dimensional base state numerically computed from a BVP, where the flow and temperature fields vary in both the x - and z -directions, and a Local Eigenvalue Problem, denoted *Local-EVP*, with a base state coming from an analytical solution (detailed in [subsection 3.3](#)) for which the system is assumed to be homogeneous, or at least slowly varying, in the x -direction. In the following subsection, each method is introduced with appropriate notation and perturbation equations.

B.1.1. Global EVP problem

We seek a complex solution for the perturbation fields in the form of normal modes in the y direction as follows

$$[u', v', w', \theta, p'] = [\hat{u}(x, z), \hat{v}(x, z), \hat{w}(x, z), \hat{\theta}(x, z), \hat{p}(x, z)] e^{\hat{s}t + ik_y y}, \quad (\text{B7})$$

Name	Method	Ra	ϵ	f	Pr	k_x	k_y	N
IVP1	IVP	10	1/8	0.9	0.1	-	-	6
IVP2	IVP	10	1/16	0.9	0.1	-	-	6
IVP3	IVP	10	1/32	0.9	0.1	-	-	6
BVP1	BVP	$\{0.98; 988\}_{20}$	1/32	0.9	0.1	-	-	16
BVP2	BVP	$\{0.49; 494\}_{20}$	1/64	0.9	0.1	-	-	16
BVP3	BVP	$\{0.24; 247\}_{20}$	1/128	0.9	0.1	-	-	18
BVP4	BVP	$\{0.12; 123\}_{20}$	1/256	0.9	0.1	-	-	18
BVP5	BVP	$\{0.06; 61\}_{20}$	1/512	0.9	0.1	-	-	20
BVP6	BVP	$\{0.03; 31\}_{20}$	1/1024	0.9	0.1	-	-	20
IVP4	IVP	1	1/32	0.9	0.1	-	-	6
IVP5	IVP	3	1/32	0.9	0.1	-	-	6
IVP6	IVP	10	1/32	0.9	0.1	-	-	6
IVP7	IVP	30	1/32	0.9	0.1	-	-	6
IVP8	IVP	100	1/32	0.9	0.1	-	-	8
IVP9	IVP	300	1/32	0.9	0.1	-	-	8
IVP10	IVP	100	1/512	0.9	0.1	-	-	8
IVP11	IVP	170	1/16	0.9	0.1	-	-	6
IVP12	IVP	5000	1/16	0.9	1.0	-	-	8
GEVP1	Global-EVP	700	1/8	[0.05;0.95]	0.1	-	[0.01; 50] ₅₀	16
GEVP2	Global-EVP	150	1/16	[0.05;0.9]	0.1	-	[0.01; 50] ₅₀	16
GEVP3	Global-EVP	31	1/32	[0.05;0.9]	0.1	-	[0.01; 50] ₅₀	16
GEVP4	Global-EVP	12	1/64	[0.05;0.9]	0.1	-	[0.01; 50] ₅₀	18
GEVP5	Global-EVP	5	1/128	[0.05;0.9]	0.1	-	[0.01; 50] ₅₀	18
GEVP6	Global-EVP	2.1	1/256	[0.05;0.9]	0.1	-	[0.6; 0.8, 1.5] ₅₀	18
GEVP7	Global-EVP	1	1/512	[0.05;0.9]	0.1	-	[0.6; 0.8, 1.5] ₅₀	20
GEVP8	Global-EVP	0.5	1/1024	[0.05;0.9]	0.1	-	[0.6; 0.8, 1.5] ₅₀	20
GEVP9	Global-EVP	$\{3.1, 980\}_{11}$	1/32	0.9	0.1	-	[0.01; 50] ₅₀	16
GEVP10	Global-EVP	$\{150; 15000\}_{11}$	1/16	0.9	0.13	-	[0.6; 2] ₅	20
GEVP11	Global-EVP	$\{150; 15000\}_{11}$	1/16	0.9	0.16	-	[0.6; 2] ₅	20
GEVP12	Global-EVP	$\{150; 15000\}_{11}$	1/16	0.9	0.2	-	[0.6; 2] ₅	20
GEVP13	Global-EVP	$\{150; 15000\}_{11}$	1/16	0.9	0.23	-	[0.6; 2] ₅	20
GEVP14	Global-EVP	$\{150; 15000\}_{11}$	1/16	0.9	0.26	-	[0.6; 2] ₅	20
GEVP15	Global-EVP	$\{150; 15000\}_{11}$	1/16	0.9	0.3	-	[0.6; 2] ₅	20
GEVP16	Global-EVP	$\{10^4; 10^6\}_{11}$	1/16	0.9	0.4	-	[0.6; 2] ₅	20
LEVP1	Local-EVP	21.27	1/16	0.9	0.1	$[-2; 2]_{48}$	$[0; 2]_{30}$	128
LEVP2	Local-EVP	$\{1.37, 10.84\}_4$	$\{1/32; 1/256\}_4$	0.9	0.1	$[-2; 2]_{48}$	$[0; 2]_{30}$	128
LEVP3	Local-EVP	3.66	1/96	0.9	0.1	$[-2; 2]_{48}$	$[0; 2]_{30}$	128
LEVP4	Local-EVP	1.10	1/320	0.9	0.1	$[-2; 2]_{48}$	$[0; 2]_{30}$	128
LEVP5	Local-EVP	10.84	1/32	0.9	0.1	$[-2; 2]_{48}$	$[0; 2]_{30}$	128
LEVP6	Local-EVP	5.46	1/64	0.9	0.1	$[-2; 2]_{48}$	$[0; 2]_{30}$	128
LEVP7	Local-EVP	2.75	1/128	0.9	0.1	$[-2; 2]_{48}$	$[0; 2]_{30}$	128
LEVP8	Local-EVP	0.68	1/512	0.9	0.1	$[-2; 2]_{48}$	$[0; 2]_{30}$	128
LEVP9	Local-EVP	0.34	1/1024	0.9	0.1	$[-2; 2]_{48}$	$[0; 2]_{30}$	128

TABLE 1. List of simulations (DNS IVP/BVP and EVP Global/Local) with physical and numerical parameters. N is the order of the spectral modes (same for each direction). The notation $[A, B]_n$ denotes an array of n linearly spaced values from A to B , inclusive, while $\{A, B\}_n$ represents an array of n values spaced evenly on a logarithmic scale from A to B inclusive.

where \hat{s} represents the complex growth rate and k_y , the wavenumber in the y -direction. Substituting this into (B1)–(B5), leads to

$$\hat{s}\hat{u} + U\hat{u}_x + W\hat{u}_z + \hat{u}U_x + \hat{w}U_z = -\hat{p}_x + Pr\mathcal{L}\hat{u}, \quad (\text{B } 8)$$

$$\hat{s}\hat{v} + U\hat{v}_x + W\hat{v}_z = -ik_y\hat{p} + Pr\mathcal{L}\hat{v}, \quad (\text{B } 9)$$

$$\hat{s}\hat{w} + U\hat{w}_x + W\hat{w}_z + \hat{u}W_x + \hat{w}W_z = -\hat{p}_z + RaPr\hat{\theta} + Pr\mathcal{L}\hat{w}, \quad (\text{B } 10)$$

$$\hat{s}\hat{\theta} + U\hat{\theta}_x + W\hat{\theta}_z + \hat{u}T_x + \hat{w}T_z = \mathcal{L}\hat{\theta}, \quad (\text{B } 11)$$

$$0 = \hat{u}_x + ik_y\hat{v} + \hat{w}_z, \quad (\text{B } 12)$$

with the operator $\mathcal{L} = (\partial_x^2 + \partial_z^2 - k_y^2)$.

B.1.2. Local EVP problem

In section 4.2.2, we use this method with a simplified 1D base state taken at a given x and neglecting the x -dependence. The vertical velocity from the base state W is also neglected. Therefore, the base flow is $\mathbf{U} = (U(z), 0, 0)$. We also account for the horizontal and vertical temperature gradient, T_x and $T_z(z)$, respectively. We seek a complex solution for the perturbation fields in a form of normal modes in the x - and y -directions as follows

$$[u', v', w', \theta, p'] = [\hat{u}(z), \hat{v}(z), \hat{w}(z), \hat{\theta}(z), \hat{p}(z)] e^{st+i(k_x x + k_y y)}, \quad (\text{B } 13)$$

where $s = \sigma + i\omega$ represents the complex growth rate and k_x, k_y are the wavenumbers in the x - and y -directions, respectively. Substituting this in (B1)–(B5) leads to

$$\lambda\hat{u} = -\hat{w}U_z - ik_x\hat{p} + Pr\hat{u}_{zz}, \quad (\text{B } 14)$$

$$\lambda\hat{v} = -ik_y\hat{p} + Pr\hat{v}_{zz}, \quad (\text{B } 15)$$

$$\lambda\hat{w} = -\hat{p}_z + RaPr\hat{\theta} + Pr\hat{w}_{zz}, \quad (\text{B } 16)$$

$$\lambda\hat{\theta} = -\hat{u}T_x - \hat{w}T_z - k^2(1 - Pr)\hat{\theta} + \hat{\theta}_{zz}, \quad (\text{B } 17)$$

$$0 = ik_x\hat{u} + ik_y\hat{v} + \hat{w}_z, \quad (\text{B } 18)$$

where $\lambda = \sigma + Prk^2 + i(\omega + Uk_x)$ and $k^2 = k_x^2 + k_y^2$.

Appendix C. Generalized Chapman & Proctor instability

C.1. Stability analysis

In this section, we examine the effect of differential heating between the top and bottom boundaries, disregarding sidewall effects and the presence of a base flow. This setup is an extension of that studied by [Chapman & Proctor \(1980\)](#) (CP), who considered various flow upper and lower boundary conditions with equal and opposite upper and lower fluxes. It corresponds to our setup with $f = 0$ and a free-slip upper boundary. Note that [Gertsberg & Sivashinsky \(1981\)](#) considered the case $f = 1$.

To address the heat flux mismatch in our case, we generalize CP's approach by examining stability for any normalized flux difference configuration. The base state is motionless and subject to a temperature profile denoted T^b . A uniform volume sink term f is added to the base state temperature equation to balance the flux mismatch, leading to the steady-state balance $\nabla^2 T^b = f$. By integrating this equation twice in the z -direction, we obtain the parabolic temperature profile

$$T^b(z) = f(\tfrac{1}{2}z^2 - \tfrac{1}{6}) - z + \tfrac{1}{2}, \quad (\text{C } 1)$$

which is the "boundary temperature" defined in (3.7) and has zero vertical average. In the subsequent analysis, we adopt the method used by CP. We seek a time-dependent

solution for a heat flux through the layer that is just above the threshold necessary for infinitesimal motion to occur. The Rayleigh number is set to $Ra = Ra_{cp} + \epsilon^2$, with $\epsilon \ll 1$ and Ra_{cp} the critical Rayleigh number. Decompose the temperature into the base state and perturbation $T = T^b + \theta$ with θ and \mathbf{u} the temperature and velocity perturbation fields, respectively. The momentum, mass and energy conservation equations for these perturbations are

$$Pr^{-1} (\mathbf{u}_t + \mathbf{u} \cdot \nabla \mathbf{u}) = -\nabla P + (Ra_{cp} + \epsilon^2) \theta \mathbf{e}_z + \nabla^2 \mathbf{u}, \quad (\text{C } 2)$$

$$\nabla \cdot \mathbf{u} = 0, \quad (\text{C } 3)$$

$$\theta_t + \mathbf{u} \cdot \nabla \theta + w T_z^b = \nabla^2 \theta. \quad (\text{C } 4)$$

CP shown that the onset of convection is a monotonically decreasing function of the wavelength, indicating that the lowest critical value of the Rayleigh number occurs for infinitely long horizontal scales. Consequently, we set $\partial_x = \epsilon \partial_X$. CP identified the relevant time scaling as $\partial_t = \epsilon^4 \partial_\tau$. Ra is just above the threshold, resulting in slow growth rates (ϵ^2), and long horizontal scales, which require $O(\epsilon^{-2})$ time to diffuse information across the domain; y -invariance is assumed and the velocity field can be written in terms of the streamfunction $\mathbf{u} = (\psi_z, 0, -\epsilon \psi_X)$. Adopting the scalings mentioned above and in addition setting $\psi = \epsilon \xi$, (C 4) and the curl of (C 2) lead to

$$\begin{aligned} Pr^{-1} [\epsilon^6 \xi_{\tau XX} + \epsilon^4 \xi_{\tau zz} + \epsilon^4 \mathcal{J}(\xi, \xi_{XX}) + \epsilon^2 \mathcal{J}(\xi, \xi_{zz})] \\ = (Ra_{cp} + \epsilon^2) \theta_X + \epsilon^4 \xi_X + 2\epsilon^2 \xi_{XXzz} + \xi_{zzzz}, \end{aligned} \quad (\text{C } 5)$$

$$\epsilon^4 \theta_\tau + \epsilon^2 \mathcal{J}(\xi, \theta) = \epsilon^2 \theta_{XX} + \theta_{zz} - \epsilon^2 \xi_X T_z^b. \quad (\text{C } 6)$$

Since odd powers of ϵ are absent in the expansion, we expand θ and ξ as power series in ϵ^2 , yielding

$$\begin{aligned} \theta &= \theta_0(X, z, \tau) + \epsilon^2 \theta_2(X, z, \tau) + O(\epsilon^4), \\ \xi &= \xi_0(X, z, \tau) + \epsilon^2 \xi_2(X, z, \tau) + O(\epsilon^4). \end{aligned} \quad (\text{C } 7)$$

We now substitute these expansions into (C 5) and (C 6). At $O(1)$, the equations yield

$$\theta_{zz} = 0 \quad \text{and} \quad Ra_{cp} \theta_X + \xi_{zzzz} = 0. \quad (\text{C } 8)$$

Since no heat flux is assumed to be transported by the perturbations at the boundaries, we have $\theta_z = 0$. Consequently, $\theta_0 = \bar{\theta}_0(X, \tau)$ leading to the streamfunction $\xi_0 = Ra_{cp} P(z) \bar{\theta}_{0X}$, which is the same equation as (3.15), with $P(z)$ defined in (3.17). This relation results from the same force balance between viscosity and buoyancy. Considering the $O(\epsilon^2)$ terms of the temperature equation yields

$$\mathcal{J}(\xi_0, \theta_0) = \theta_{0XX} + \theta_{2zz} - \xi_{0X} T_z^b. \quad (\text{C } 9)$$

Substituting the leading-order solution leads to

$$\theta_{2zz} = -Ra_{cp} (\bar{\theta}_{0X})^2 P' - \bar{\theta}_{0XX} [1 - Ra_{cp} P T_z^b]. \quad (\text{C } 10)$$

By averaging (C 10) over the height and applying the boundary conditions on θ , we obtain

$$\int_0^1 \theta_{2zz} \, dz = [\theta_{2z}]_{-1}^1 = 0, \quad (\text{C } 11)$$

since $P(-1) = P(1) = 0$. Seeking a non-zero leading order for the temperature field implies

$$\int_0^1 [1 - Ra_{cp} P T_z^b] \, dz = 0. \quad (\text{C } 12)$$

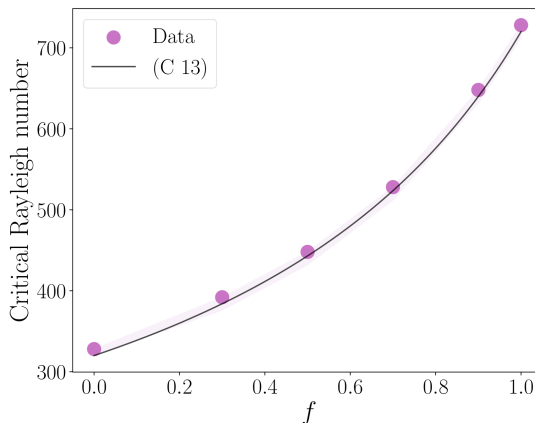


FIGURE 17. Critical Rayleigh number for the generalized Chapman & Proctor instability as a function of the normalized flux difference.

This leads to

$$\mathcal{Ra}_{cp} = \frac{2880}{9 - 5f}, \quad (\text{C } 13)$$

which corresponds to the definition of \mathcal{Ra}_{cp} in (3.23). When $f = 0$, $\mathcal{Ra}_{cp} = 320$, corresponding to 16 times the value of 20 given in CP for mixed boundary conditions, also found by Soward *et al.* (2022). In CP, the Rayleigh number is based on the half-height, so the height's fourth power in Ra results in a factor of 16. Similarly, when $f = 1$, we recover the threshold value of 720 found by Gertsberg & Sivashinsky (1981). It is noteworthy that the threshold increases as the normalized flux difference decreases. For $f \neq 0$ fixed, this occurs because the heat flux decreases linearly with altitude, resulting in a fluid particle perceiving less buoyancy as it rises. Consequently, the buoyancy force experienced by the particle diminishes, making it more likely to be stabilized by diffusive effects.

To verify the validity of (C 13), we perform DNS simulations of the CP configuration, using the IVP-method, in a 2D box with an aspect ratio of 32 and periodic boundaries in the x -direction. We include a uniform volume heat sink term f in the temperature equation and fix the heat fluxes to 1 and $1 - f$ to the bottom and the top respectively. Figure 17 shows the marginal stability curve i.e the \mathcal{Ra}_{cp} as a function of f . Each data point was obtained by initiating a simulation from an initial condition with no flow and a zero temperature field in the domain, and then identifying the Ra value for which exponential growth in velocity magnitude first occurs. We observed no significant dependence on the aspect ratio. The numerical data align perfectly with (C 13).

C.2. Flow stabilization effect

The generalized Chapman–Proctor instability can initially emerge in the system but may be suppressed during the transient phase of base flow development. Figure 18 presents snapshots from a 3D IVP showing the temperature field (top) and the velocity amplitude (bottom) at successive times. The simulation parameters are $\epsilon = 1/16$, $Ra = 5000$, and $f = 0.9$. The Prandtl number is fixed at $Pr = 1$ to ensure that the base state remains stable with respect to the three-dimensional instability analyzed in section 4. We recall that IVP simulations are initiated with a quiescent fluid and a uniform temperature field $T = 0$, where small temperature perturbations of amplitude

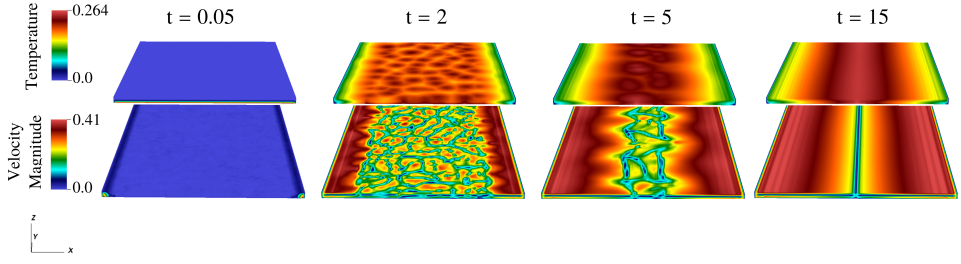


FIGURE 18. Snapshots of the 3D temperature (top) and velocity magnitude (bottom) fields, at various times.

10^{-3} are introduced, leading to thermal convection growth during a transient phase, as shown in Figure 18. We choose a sufficiently large Ra to be supercritical for the Chapman & Proctor instability (threshold at $Ra = 640$ for $f = 0.9$). At the beginning, when the system is close to the initial conditions, the flow from the sidewall has not yet expanded throughout the entire domain and the temperature is mainly uniform. As time progresses, the Chapman & Proctor instability emerges, forming convection rolls ($t = 2$). At this stage, the base flow has not yet propagated throughout the domain. As this flow advances towards the centre, the convection rolls disappear, the system stabilizes ($t = 5$) and becomes completely stable (we observe exponential decay of all fluctuations) when the steady state is reached ($t = 15$).

REFERENCES

- BATCHELOR, G. K. 1954 Heat transfer by free convection across a closed cavity between vertical boundaries at different temperatures. *Quart. Appl. Math.* **12**, 209–233.
- BRUYN, J., BODENSCHATZ, E., MORRIS, S., TRAINOFF, S., HU, Y., CANNELL, D. & AHLERS, G. 1996 Apparatus for the study of Rayleigh–Bénard convection in gases under pressure. *Rev. Sci. Instrum.* **67**, 2043–2067.
- BURNS, K. J., VASIL, G. M., OISHI, J. S., LECOANET, D. & BROWN, B. P. 2020 Dedalus: A flexible framework for numerical simulations with spectral methods. *Physical Review Research* **2**, 023068.
- BUSSE, F. H. 1972 The oscillatory instability of convection rolls in a low prandtl number fluid. *J. Fluid Mech.* **52**, 97–112.
- BUSSE, F. H. 1978 Non-linear properties of thermal convection. *Rep. Prog. Phys.* **41**, 1929.
- BUSSE, F. H. & CLEVER, R. M. 1979 Instabilities of convection rolls in a fluid of moderate prandtl number. *J. Fluid Mech.* **91**, 319–335.
- CALDWELL, D. R. 1970 Non-linear effects in a Rayleigh–Bénard experiment. *J. Fluid Mech.* **42**, 161–175.
- CARÉNINI, L., FICHOT, F. & SEIGNOUR, N. 2018 Modelling issues related to molten pool behaviour in case of in-vessel retention strategy. *Ann. Nuclear Energy* **118**, 363–374.
- CHANDRASEKHAR, S. 1981 *Hydrodynamic and Hydromagnetic Stability*. Dover.
- CHAPMAN, C. J. & PROCTOR, M. R. E. 1980 Nonlinear Rayleigh–Bénard convection between poorly conducting boundaries. *J. Fluid Mech.* **101**, 759–782.
- CLEVER, R. M. & BUSSE, F. H. 1990 Convection at very low Prandtl numbers. *Phys. Fluids A* **2**, 334–339.
- CORMACK, D. E., LEAL, L. G. & IMBERGER, J. 1974 Natural convection in a shallow cavity with differentially heated end walls. Part 1. Asymptotic theory. *J. Fluid Mech.* **65**, 209–229.
- DANIELS, P. G., BLYTHE, P. A. & SIMPKINS, P. G. 1987 Onset of Multicellular Convection in a Shallow Laterally Heated Cavity. *Proc. Ro. Soc. Lond. (A)* **411**, 327–350.
- DANIELS, P. G. & GARGARO, R. J. 1993 Buoyancy effects in stably stratified horizontal boundary-layer flow. *J. Fluid Mech.* **250**, 233–251.

- DEVILLE, M. O., FISCHER, P. F. & MUND, E. H. 2002 *High-Order Methods for Incompressible Fluid Flow*. Cambridge University Press.
- DIXIT, G., BUKHARI, S. F. & PATNE, R. 2024 Linear dynamics of a thick liquid layer subjected to an oblique temperature gradient. *J.Fluid Mech.* **987**, A32.
- FISCHER, P. F. 1997 An overlapping Schwarz method for spectral element solution of the incompressible Navier–Stokes equations. *J.Comp.Phys.* **133**, 84–101.
- GANZAROLLI, M & MILANEZ, L. F 1995 Natural convection in rectangular enclosures heated from below and symmetrically cooled from the sides. *Int.J.Heat Mass Transf.* **38**, 1063–1073.
- GERTSBERG, V. L. & SIVASHINSKY, G. I. 1981 Large Cells in Nonlinear Rayleigh–Bénard Convection. *Prog.Theore.Phy.* **66**, 1219–1229.
- GILL, A. E. 1966 The boundary-layer regime for convection in a rectangular cavity. *J.Fluid Mech.* **26**, 515–536.
- GOLUBITSKY, M., SWIFT, J.W. & KNOBLOCH, E. 1984 Symmetries and pattern selection in Rayleigh–Bénard convection. *Physica D* **10**, 249–276.
- HART, J.E. 1983 Low prandtl number convection between differentially heated end walls. *Int.J.Heat Mass Transf.* **26**, 1069–1074.
- KRISHNAMURTI, R. 1970 On the transition to turbulent convection. Part 1. The transition from two- to three-dimensional flow. *J.Fluid Mech.* **42**, 295–307.
- LE GUENNIC, C., SKRZYPEK, E., SKRZYPEK, M., BIGOT, B., PEYBERNES, M. & LE TELLIER, R. 2020 Synthesis of wp2.3 results on the metallic layer and new correlations. In *Proceedings of International Seminar on In-vessel retention: outcomes of IVMR project*.
- MEYER, A.AND YOSHIKAWA, H. N. & MUTABAZI, I. 2015 Effect of the radial buoyancy on a circular Couette flow. *Phys. Fluids A* **27**, 114104.
- MUTABAZI, I. & BAHLOUL, A. 2002 Stability analysis of a vertical curved channel flow with a radial temperature gradient. *Theor.Comp.Fluid Dyn.* **16**, 79–90.
- OISHI, J. S., BURNS, K. J., CLARK, S. E., ANDERS, E. H., BROWN, B. P., VASIL, G. M. & LECOANET, D. 2021 eigentools: A Python package for studying differential eigenvalue problems with an emphasis on robustness. *J.Open Source Software* **6**, 3079.
- ORTIZ-PÉREZ, A.S. & DÁVALOS-OROZCO, L.A. 2014 Convection in a horizontal fluid layer under an inclined temperature gradient for Prandtl numbers $Pr > 1$. *Int.J.Heat Mass Transf.* **68**, 444–455.
- ORTIZ-PÉREZ, A.S. & DÁVALOS-OROZCO, L.A. 2015 Convection in a horizontal fluid layer under an inclined temperature gradient with a negative vertical Rayleigh number. *Int.J.Heat Mass Transf.* **90**, 1214–1220.
- PATNE, R. & ORON, A. 2022 Buoyancy instabilities in a liquid layer subjected to an oblique temperature gradient. *J.Fluid Mech.* **937**, A11.
- PEDLOSKY, J. 2013 *Geophysical Fluid Dynamics*. Springer, New York.
- REIN, F., CARÉNINI, L., FICHOT, F., FAVIER, B. & LE BARS, M. 2023 Interaction between forced and natural convection in a thin cylindrical fluid layer at low prandtl number. *J.Fluid Mech.* **977**, A26.
- REIN, F., CARÉNINI, L., FICHOT, F., FAVIER, B. & LE BARS, M. 2025 Experimental study of the convection in a thin cylindrical gas layer with imposed bottom and top fluxes and imposed side temperature. *J.Fluid Mech.* **1006**, A22.
- REIN, F., FICHOT, F., CARÉNINI, L., LE BARS, M. & FAVIER, B. 2024 New correlations for focusing effect evaluation of the light metal layer in the lower head of a nuclear reactor in case of severe accident. *Nucl. Eng.* **428**, 113540.
- SOWARD, A.M., ORUBA, L. & DORMY, E. 2022 Bénard convection in a slowly rotating penny-shaped cylinder subject to constant heat flux boundary conditions. *J.Fluid Mech.* **951**, A5.
- THEOFANOUS, T.G., LIU, C., ADDITON, S., ANGELINI, S., KYMÄLÄINEN, O. & SALMASSI, T. 1997 In-vessel coolability and retention of a core melt. *Nucl.Engi.Design* **169**, 1–48.
- WEBER, J. E. 1978 On the stability of thermally driven shear flow heated from below. *J.Fluid Mech.* **87**, 65–84.
- YOSHIKAWA, H., NAGATA, M. & MUTABAZI, I. 2013 Instability of the vertical annular flow with a radial heating and rotating inner cylinder. *Phys. Fluids A* **25**, 114104.